2-10-2021

Establishing a mechanistic link between disturbed flow and aneurysm formation in a 3D cerebral bifurcation model

Nesrine Bouhrira
Rowan University

ESTABLISHING A MECHANISTIC LINK BETWEEN DISTURBED FLOW AND ANEURYSM FORMATION IN A 3D CEREBRAL BIFURCATION MODEL

by

Nesrine Bouhrira

A Thesis

Submitted to the
Department of Biomedical Engineering
College of Engineering
In partial fulfillment of the requirement
For the degree of
Doctor of Philosophy
at
Rowan University
January 2021

Thesis Chair: Peter Adam Galie, Ph.D.

Dedications

To my parents, fiancé and family, for their love and support.

Acknowledgements

Abstract

Nesrine Bouhrira
ESTABLISHING A MECHANISTIC LINK BETWEEN DISTURBED FLOW AND
ANEURYSM FORMATION IN A 3D BIFURCATION MODEL.
2020-2021
Peter A. Galie
Doctor of Philosophy in Biomedical Engineering

The effect of disturbed flow profiles on the endothelium have been studied extensively in systemic vasculature, but less is known about the response of the blood-brain barrier (BBB) to these flow regimes. Here we investigate the effect of steady and pulsatile disturbed flow on the integrity of the BBB using a three-dimensional, perfusable bifurcation model consisting of a co-culture of endothelial cells with mural and glial cells. Experimental flow patterns predicted by computational fluid dynamics mimic in vivo flow regimes, specifically the presence of a recirculation zone immediately downstream of the bifurcation reveal periodic changes in the instantaneous shear stress along the channel wall. Dextran permeability assays and immunostaining with markers for tight junctions show that barrier disruption is significantly greater in areas of disturbed flow compared to fully developed regions downstream of the bifurcation. RNA sequencing found differences in gene expression between the disturbed and fully developed regions, and lumican which has been implicated in ECM organization and collagen fibrillogenisis was shown to be significantly upregulated in the fully developed region. Furthermore, the downregulation of the protein is associated with barrier breakdown. Overall, disturbed flow-induced disruption of the blood-brain barrier suggests that flow-mediated mechanisms may contribute to vascular pathologies in the central nervous system.

Table of Contents

Table of Contents (Continued)

Table of Contents (Continued)

List of Figures

List of Tables

Chapter I

Introduction

A key determinant in brain pathology and homeostasis is the impact of blood flow regimes on the integrity of the blood-brain barrier (BBB). Numerous studies have validated that the integrity of the BBB is sensitive to the wall shear stress applied by blood flow. While physiological wall shear stress has been shown to maintain barrier integrity and brain homeostasis, low levels of fluid shear stress have been associated with higher BBB permeability and disruption of its integrity [1]. The breakdown of the BBB has been associated with several neurological disorders including but not limited to stroke, Alzheimer's disease, and traumatic brain injury [2-4]. Furthermore, the integrity of BBB is important at all levels of the vascular tree within the CNS[5], including the large arteries in the subarachnoid space. At these locations, vessels are characterized by temporally and spatially varying wall shear stress[6] due to the pulsatility of blood flow[7] and the tortuosity of the vascular bed at those locations [8, 9]. In addition, there is a potential of disturbed flow regions at these locations due to flow separation from the wall at vascular bifurcations. These variations have been associated with abnormal flow patterns, non-physiological wall shear stress profiles and therefore breakdown of the BBB. Several studies have associated the BBB dysfunction caused by altered blood flow regimes at these locations with aneurysm initiation, suggesting that altered shear stress may disrupt the BBB at these locations due to the presence of recirculation eddies caused by disturbed flow.

There is growing evidence suggesting that aneurysm formation is widely associated with tight junction disruption as well as degradation of the basement membrane proteins[10, 11]. Furthermore, there are several signaling mechanisms that could

1

mediate the response to disturbed flow, including mechanosensitive small GTPases, that

upon activation, have been implicated in the regulation of the BBB through the RhoA-

ROCK signaling pathway [12, 13]. Moreover, RhoA activation is associated with tight

junction maintenance as well as interactions with extracellular matix (ECM) components,

providing further evidence that the small GTPase may mediate endothelial

mechanotransduction. Therefore, interrogating the impact of time-dependent flow

patterns on the endothelial cells response inside complex vascular geometries mimicking

cerebral vasculatures can elucidate the molecular mechanisms underlying the

mechanotransduction of disturbed flow on the BBB integrity and function.

Previous studies have demonstrated that the phenotype of endothelial cells in

systemic vasculature is markedly different than in the brain [14-16]. However, the effect of

altered shear stress on the integrity of the BBB has not been studied as thoroughly[17-19].While endothelial cells in the systemic vasculature can withstand hemodynamic stress

and maintain vascular integrity when exposed to laminar flow [20-22], disturbed flows in the

separation zone [9, 23, 24] and reattachment point [25-27] contribute to vasculature dysfunction

and altered gene expression [28]. In addition, disturbed flow has been shown to destabilize

cell-cell and cell-ECM contacts adjacent to bifurcations[21, 22, 27, 29]. Such destabilization in

the brain would lead to barrier breakdown. Yet, the impact of time-dependent disturbed

fluid flow on the integrity of the BBB in a geometry that mimics cerebral bifurcation has

yet to be investigated. Therefore, there is a need for a 3-dimensional (3D) BBB model to

interrogate the response of endothelial cells to the different flow regimes. Previous

studies have used *in vitro* models to recreate the fluid mechanics of the endothelial

microenvironment[25, 26]. In contrast to animal models, *in vitro* models provide a higher

level of control over fluid flow regimes exposed to the endothelium. These systems have applied both steady and pulsatile flow to cerebral endothelial cells in both two-dimensional (2D)[2, 27, 28] and three-dimensional (3D) geometries[30]. In contrast, 3D bifurcation models that create disturbed flow regimes in geometries that are more similar to *in vivo* vasculature, are yet to be investigated.

Therefore, the approach described here involves a cerebral bifurcation model constructed inside a microfluidic device to establish a mechanistic link between disturbed flow and aneurysm formation in a platform that mimics the brain microenvironment. The model includes a 3D co-culture of three different cell types. Here, both glial and mural cells are incorporated into a co-culture model with the endothelium to approximate the vessel bore that experiences disturbed flow *in vivo*, since larger arteries exhibit a prominent mural layer that supports the augmented pressure differences incurred by higher flow rates. An annulus of smooth muscle cells surrounds the endothelial lumen, and the annulus itself is surrounded by an astrocyte-seeded hydrogel, to approximate the arrangement of these cells *in vivo* [31]**.** Furthermore, the vessels are patterned within a microfluidic device that is capable of applying different fluid flow levels with a sufficiently high Reynolds number to separate from the wall of the endothelial lumen, yielding an experimental setup that can directly interrogate the response of the BBB to altered shear stress profiles. Here, the desired physiological pulsatile waveform was successfully generated using a low-cost linear actuator and components fabricated from a common fused deposition modeling (FDM) 3D-printer**.** The system divides the task of flow waveform generation between two components: the peristaltic pump which generates steady flow and a linear actuator generating oscillations to recreate the systolic

and diastolic pressures. The model described here provides a platform to study the effect of time dependent altered shear stress on the integrity of the BBB in a 3D in vitro setting that mimics several aspects of the *in vivo* microenvironment of the brain vasculature.

Throughout the studies, the flow characterization was conducted using both experimental and computational fluid dynamic models. The cellular response was quantified using immunofluorescence, immunoblotting, Permeability assays, Bromodeoxyuridine / 5-bromo-2'-deoxyuridine (Brdu) assays and rheology. In addition, RNA sequencing along with bioinformatics was used to determine differential gene expression in the endothelium exposed to steady flow. Finally, gene knockdown was utilized to modulate the expression of the proteoglycan lumican to probe its impact on the integrity of the BBB and the activation of the small-GTPases. This dissertation is organized into five chapters. Chapter 1 is the introduction. Chapter 2 represents the background information on the BBB and the different flow regimes as well as the current models used to study the impact of flow on the endothelium in the brain. It finally introduces the specific aims for the dissertation. Chapter 3 details the experimental approach utilized, the computational fluid dynamics models and the in vitro experimental setup. Chapter 4 summarizes the results investigating the impact of both steady and pulsatile flow on the BBB integrity. It also details the RNA sequencing results to determine the differentially expressed genes in the endothelium exposed to steady flow. Finally, it underlines the mechanistic link between the BBB disruption and aneurysm formation using gene knockdown. Finally, Chapter 5 summarizes all the experimental approach and results with a discussion of the accomplished work.

<center>**Chapter II**</center>

<center>**Background**</center>

2.1. The Blood-Brain Barrier (BBB)

2.1.1. Introduction to the BBB. The blood-brain barrier is a complex biological barrier that separates select blood components from the parenchyma of the brain, which along with the spinal cord make up the central nervous system (CNS)[32-34]. It plays a key role in maintaining brain homeostasis[35-37] as well as facilitating the transport of nutrients and other solutes through the CNS[37]. The BBB is present in all scales of blood vessels in the brain[38] and is formed by endothelial cells (ECs) lining the brain vasculature, pericytes and astrocyte end feet[35], and a basal membrane that separates ECs from pericytes, and astrocytes[39, 40]**.** The development and maintenance of the BBB are governed by cellular and non-cellular elements that interact with the ECs. While, astrocytes, pericytes, and the extracellular matrix (ECM) components provide both structural and functional support to the BBB, the endothelial cells exhibit a unique phenotype, making the brain capillaries 50 to 100 times tighter than peripheral microvessels as a result of tightly sealed monolayer of endothelial cells with tight junctions (TJ) and adherens junctions (AJ)[41]. In addition, the basal membrane and astrocyte end-feet contribute to BBB function and integrity by regulating the expression of specific TJ proteins and other BBB transporters.

Brain tight junctions have different biological functions and are composed of integral membrane proteins including claudins and occludins[42 43]**,** which are involved in intercellular contacts and interactions with cytoplasmic scaffolding proteins such as zonula occludens-1(ZO-1) proteins (Fig.1) , actin cytoskeleton and associated proteins,

<center>5</center>

such as protein kinases, small GTPases[44] and heterotrimeric G-proteins[45]. They serve to limit the BBB permeability and increase the barrier's electrical resistance by limiting transport through cell-cell junctions.
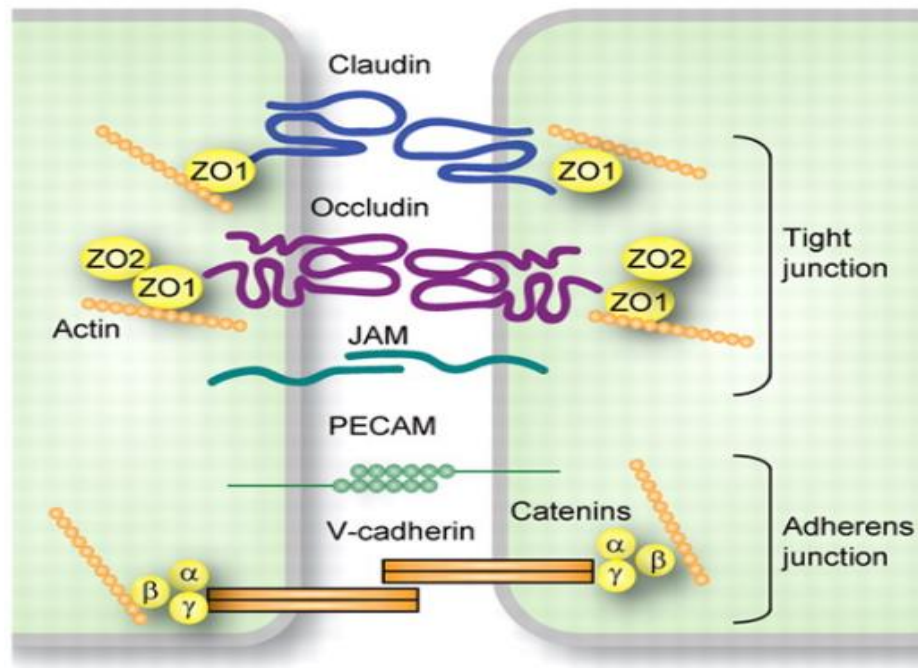
*Figure 1.*Schematic of the tight junctions between two endothelial cells

2.1.2. The impact of shear stress on BBB integrity. Several in vitro studies have shown that formation and maintenance of the BBB in microvascular models requires exposure to fluid shear stress[1, 15]. In fact, the wall shear stress applied by the blood flow has been shown to have a detrimental effect on endothelial cell function,

morphology, gene expression and barrier integrity through the regulation of several tight junction proteins. Several studies have shown that exposure to capillary-like shear stress levels (6.2 dynes/cm^2) increases the RNA levels of a variety of tight and adherens junction components such as zonula occludens-1 (ZO-1), Claudin 3 and 5, cadherins, catenin α2 and β1, and actin α2[1, 46, 47] in addition to reducing barrier permeability and promoting actin cytoskeleton reorganization [42, 48, 49]. However, low levels of fluid shear stress have been associated with lower expression of tight junction proteins, breakdown of the barrier and higher permeability.

2.1.3.   The impact of the vasculature topology on flow and disease. The BBB exists at all levels of the vascular tree within the CNS (Fig. 2)[5] including the arteries and arterioles, the dense capillary bed, the venules and veins. Therefore, the integrity of the barrier is crucial not only in the microvasculature within the brain parenchyma, but also in the larger pial and cerebral arteries in the subarachnoid space [89]. In these vessels, the BBB includes an additional layer of smooth muscle cells and is exposed to a time varying flow and higher Reynolds numbers. There is a potential for disturbed flow, especially at arterial bifurcations due to the tendency to separate from the wall at these locations [20, 50]. In addition, the vascular topologies exacerbate the blood flow patterns at these locations[6] and expose the endothelium to a time-dependent shear stress field varying is magnitude during the cardiac cycle, with periodic appearance of flow separation zones, yielding oscillating wall shear stress profiles[6, 9]. Therefore, changes in the blood flow profiles could trigger BBB and TJ disruption, and lead to increased extravasation of immune cells across the BBB, leading to decreased CNS protection and potentially to brain inflammation.
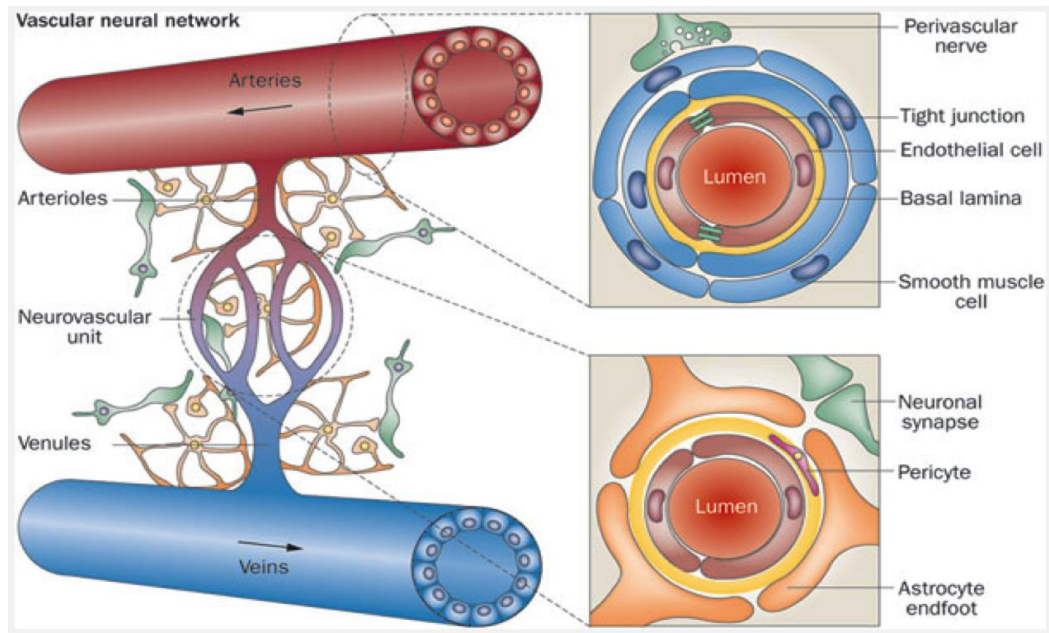
*Figure 2.*The vascular neural network [51].

Changes in blood flow have been associated with BBB disruption in several neuropathological conditions including dementia and Alzheimer's, epilepsy and ischemic stroke [2-4]. In addition, evidence that the incidences of aneurysms and endothelial dysfunction are higher at bifurcations in cerebral arteries [52, 53] suggests that altered shear stress may disrupt the BBB at these locations.

Several studies investigating the impact of wall shear stress on the vasculature in the brain demonstrated that flow dynamics play an important role in the initiation, growth, and rupture of cerebral artery aneurysms[54-56]. In fact, the wall shear stress applied on the bifurcation has been shown to play a huge role in aneurysm initiation and rupture. Studies

8

demonstrated that larger bifurcation angles lead to abnormally enhanced hemodynamic stresses and enlarged zones of direct flow impingement and recirculation eddies[54]. In addition, a study conducted by Hassan et.al [55] investigating the response of human umbilical vein endothelial cells to hemodynamic stresses in an actual patient-specific cerebral aneurysm model showed that the aneurysmal dome experiences relatively low WSS compared with the impingement zone at the distal aneurysm neck and downstream parent vessel. Furthermore, the study showed that high levels of shear stress profiles impacted endothelial cells morphology and orientation. These results indicate that abnormal flow profiles lead to the dysfunction of the endothelial cells which in return is associated with cerebral aneurysms.

2.1.4. Models of the BBB. To better understand the physiology of brain vasculature, there is a need to develop experimental models that mimic the properties and function of the BBB or directly perform experiments in living organisms. Ideal BBB models mimic the cell types and distribution within the in vivo microenvironment and have high selective permeability to different substances [35]. Several BBB models have been developed in the past including in vivo, static, and perfusable 2D and 3D models.

2.1.4.1. In vivo models. In vivo BBB models were investigated in the past by performing experiments in animals. The main advantage of these models is that the experiment occurs under natural conditions and can generate large amounts of reliable data [57]. In addition, they closely mimic the complexity of human physiology and the brain microenvironment. In these models, the function of the BBB is studied using several methods consisting of, intravenous injection and brain perfusion [58]. However, the main disadvantage of the in vivo studies is the complexity of the in vivo microenvironment that

prohibits robust control of the fluid dynamics environment. In addition, animal-to-animal

variability represents an additional limitation that makes in vitro experiments an

alternative for studying the function and response of the BBB to flow.

2.1.4.2. ***Current Experimental BBB models***. *In vitro* models for

cerebrovascular studies of the BBB started to emerge in the early 1990s as potential new

research tools complementary to in vivo and human studies. These models are a major

focus in research due to their ability to replicate the vascular properties and the brain

microcapillaries microenvironment. They provide highly controllable environments in

vitro to manipulate cells and tune specific physiological and experimental stimuli

difficult to reproduce in vivo. These models include static culture systems, flow-based

systems, two-dimensional and three-dimensional extracellular matrix-based models. The

primary caveat of these models is the inability to fully recreate the complexity of the in

vivo microenvironment

2.1.4.2.1. Static models. Previous studies have relied on static BBB models

that feature either endothelial cells or multiple cell types cultured on semi-permeable

microporous inserts [59]. The mono-culture models represent a simplistic reconstruction of

the BBB and therefore do not capture the complex architecture of the BBB including the

interaction with other cell types, which is crucial for the properties and functions of the

BBB. In co-culture experimental models, brain microvasculature endothelial cells

(BMECs) and other BBB cell types such as astrocytes and pericytes have been cultured

on different sides of a membrane [60]. While, the addition of astrocytes has been shown to

facilitate the formation of tight junctions and the overall expression of BBB features,

these models lack a number of necessary features for the development of BBB properties

in vitro. They exhibit high permeability due to the absence of physiological stimuli which significantly limits the ability of the vascular endothelium to develop and maintain the BBB properties and functions observed *in vivo* [61, 62]. Lacking the continuous exposure to wall shear stress, affects the integrity of the barrier and causes major differences in cell morphology and barrier permeability when compared with in vivo models [63].

2.1.4.2.2. Perfusable BBB models. Recent advances in vascular patterning have enabled the development of in vitro models that can closely mimic *in vivo* geometries and microenvironments [64]. These advances can build upon previous BBB models that have relied on two-dimensional geometries [65, 66] or used three-dimensional models that mimic small diameter vessels by co-culturing endothelial cells with astrocytes or pericytes [67, 68]. Several models were created using microfluidic chips and a variety of techniques, such as the gelation of ECM around a removable template rod [69, 70], soft lithography[71], and 3D printing[72]. However, microfluidic chip models exhibit unique advantages in the BBB research due to their ability to mimic the in vivo microenvironment. These devices can be tuned to meet specific experimental requirements due to their ability to mimic the size of microvascular structures in vivo and allow for fluid control. Therefore, these models can be used to interrogate cell morphology, and permeability of the BBB in response to fluid flow.

While the current 3D BBB models showed their utility to study and characterize the role of the BBB in the pathogenesis of major neuroinflammatory diseases, they lack a physiologically relevant diameter to model large arteries in the subarachnoid space that is necessary to study aneurysm formation. They are also limited due to the inability to support high Reynolds numbers required to induce flow separation (Re > 100) and sustain high

fluid flow levels for a continuous period of time (e.g. 24 h). Moreover, current in vitro models of cerebral vasculature are inadequate for studying the effects of disturbed fluid flow due to a lack of three-dimensionality, dependence on synthetic meshes to support the endothelium and the lack of smooth muscle cells in the co-culture model.

2.1.5. Endothelial cells used for BBB models. Several endothelial cells types have been utilized to replicate the BBB characteristics (Table.1). Initially, in vitro models relied on primary brain microvasculature endothelial cells (BMECs), however these cells are post-mitotic and difficult to isolate. Therefore, several human and animal cell lines have been developed to model the BBB to overcome the limitations of using BMECs. Among these cells, cultured human brain (human brain microvascular endothelial cells, HBMECs) and non-brain HUVECs vascular cells became available in the early 1980s and exhibit excellent characteristics for the study of the developmental and pathophysiological processes of the BBB. Unfortunately, the high level of difficulty associated with isolating these cells from the brain tissue as well as their rapid senescence, made their use costly and time consuming. Therefore, immortalized cell lines from diverse origins have been developed, in the BBB research and include hCMEC/D3, a human adult cerebral microvascular endothelial cell line[73] .These cell lines have many advantages over primary cultures and other cell types, which include being easy to grow in addition to retaining their differentiating properties after several passages with a reduced time to reach confluency. Therefore, they decrease the workload, cost, and labor. But some studies reported that immortalized cell lines may lose their phenotype after numerous passages, resulting in a leaky barrier[74].

12

Table 1

Summary of previously used endothelial cells to model the BBB

Cells	Advantages	Disadvantages
Primary[75 76-78]	-Close initial resemblance to in vivo conditions	-Post-mitotic -Difficult to obtain
Immortalized [17, 79, 80]	-Stable over numerous passages	-Could lose their phenotype after numerous passages -Genetically modified
IPSC- derived [81-83]	- Renewable source -Patient specific [84-88]	-Require differentiation and thorough characterization -Current protocols do not result in a true representation of the BBB phenotype [89]
HUVECS	-Can be isolated in large amounts -Easy to obtain	-Not a true representation of the BBB phenotype
Fetal derived cells [90-93]	-More representative model -TJP expression is characteristic of mature barrier properties	-Generate controversy from ethics committees

2.2. Problem Statement And Specific Aims

The following dissertation develops and characterizes an in vitro vascular model of a cerebral artery that controls both the mechanical and biochemical environment of a co-culture of endothelial cells, smooth muscle cells, and astrocytes. The model will interrogate the overall hypothesis that disturbed flow promotes aneurysm formation by modifying endothelial gene expression profiles related to extracellular matrix remodeling and the

formation of tight junctions. The proposed study is organized into the following specific aims:

Aim 1: Analyze the effects of disturbed flow on the integrity of the blood-brain barrier adjacent to arterial bifurcations. Aim 1 assesses the effects of disturbed fluid flow from both steady and pulsatile flow on blood-brain barrier (BBB) integrity using immunofluorescence and dextran permeability assays. These studies evaluate the hypothesis that altered shear stress exerted by disturbed flow disrupts endothelial tight junctions.

Aim 2: Determine differentially expressed genes in the endothelium exposed to altered flow regimes using RNA sequencing of vessels exposed to both steady and pulsatile flow. After interrogating the effect of flow on the BBB, Aim 2 compares gene expression profiles in regions of the vessel exposed to different flow regimes (fully developed, disturbed, impingement, and a static control) using next generation sequencing methods (RNA-seq). The proposed approach tests the hypothesis that disturbed flow alters the expression of genes in endothelial cells associated with extracellular matrix remodeling and organization and tight junction formation.

Aim 3: Interrogate the molecular mechanisms underlying the endothelial response to disturbed flow. Aim 3 focuses on measuring the activation of small GTPases associated with mechanotransduction and barrier regulation, including RhoA and Rac1, to provide insight into signaling mechanisms associated with disturbed flow. These studies will also use the findings of the previous aim regarding differentially expressed genes to investigate mechanistic effects. Overall, this aim addresses the hypothesis that the expression of

extracellular matrix components altered during exposure to disturbed flow mediates autocrine signaling mechanisms associated with aneurysm formation.

Chapter III

Methods and Materials

3.1. Experimental Methods

3.1.1. Vessel fabrication.

3.1.1.1. Microfabrication of microfluidic device. Polydimethylsiloxane (PDMS) microfluidic devices were manufactured by soft lithography using a previously described protocol [15]. Briefly, SU-8 2025 photoresist (MicroChem) was deposited on a silicon wafer and exposed to a UV source through a mask with the desired geometry. The inlet was positioned at an angle of 45 degrees to induce separated flow within the range of Reynolds numbers appropriate for modeling arterial blood flow (Re = 50-200). PDMS was used to cast negative and positive molds of the design and to pattern devices on 22mm x 40mm glass cover slips. The hydrogel reservoir had dimensions of 6.5 x 6.5-mm and a height of approximately 2-mm. Prior to adding a hydrogel to the device, the reservoir was filled with 5M sulfuric acid, washed with distilled water, and incubated in dilute type I collagen (20 µg/mL) to facilitate hydrogel attachment to PDMS [94]. The devices were then sterilized using short wavelength UV prior to channel seeding.

3.1.1.2. Cell culture. Normal human astrocytes (NHA) (Lonza) were thawed at passage 5 and cultured for 10 days in astrocyte growth medium (AGM) (Lonza) prior to seeding in the microfluidic device. Human Coronary Arterial Smooth Muscle Cells (HCASMC) (Sigma) were also thawed at passage 5 and cultured in smooth muscle growth medium (Sigma) until confluency, then passaged and cultured in 6 well plates using smooth muscle cell differentiation medium (Sigma) for 10 days prior to vessel fabrication.

16

Additionally, human cerebral microvascular endothelial cells (HCMEC/d3) received at passage 19 (gifted from Dr. Robert Nagele's laboratory) were cultured and expanded on tissue culture plates coated with 1% gelatin in EGM-2 modified with CD lipid concentrate and HEPES buffer according to a previously described protocol [17].

       3.1.1.3.   ***In vitro vessel fabrication.***   Normal human astrocytes (NHA) were seeded at a density of 1 million cells per mL in a 10 mg/mL collagen, 1.33 mg/mL hyaluronan (HA) and 1 mg/mL Matrigel hydrogel formulation used in a previous study[95]. After injecting the gel directly into the reservoir, an 18-g needle coated with 0.1% Bovine Serum Album (BSA) (Sigma) was inserted into the device through the 18-g needle guide. After waiting 20 minutes to allow for gel polymerization, the needle was pulled to create a cylindrical void, and AGM was added through Port 1 to maintain cell viability. HCASMC were then seeded into a 10 mg/mL collagen and 1 mg/mL Matrigel composite hydrogel at a density of 1 million cells per mL. The AGM was aspirated prior to injection of the hydrogel through Port 3, and a 20-g needle coated in 0.1% BSA in PBS was inserted inside the void lumen using the 20-g needle guide. The 20-g needle was then removed, leaving a final cylindrical void and surrounding annulus. HCMEC/d3 were resuspended in EGM-2 at a density of 5 million per mL. 15 μL of the HCMEC/d3-containing solution was injected into the channel through Port 1 and incubated for 10 minutes, yielding a seeding density of approximately 150,000 cells per cm^2. This process was repeated for an additional 10 minutes after inverting the device to assure uniform lumen coverage throughout the channel. Silicone grease was used to close the 18-g needle guide and Port 2. Port 2 was blocked to increase the length of the recirculation zone along the cell-seeded channel by effectively closing the non-cell seeded branch of the bifurcation. Devices were left in static

17

conditions for 2 days submerged in EGM-2 to ensure cell spreading and viability prior to exposure to flow or static conditions. A total of 29 vessels were fabricated using this method (three for flow validation, six for proliferation assays and viability assays, five for immunohistochemistry, and nine for permeability testing).

3.1.1.4. LifeAct transfection. P3 HCASMC cultured in SMC growth medium (Cell Applications) were transfected with RFP LifeAct lentivirus (Ibidi) at a MOI of 2.5. Following 48 hours of incubation with the virus RFP positive cells were selected by adding 5 mg/mL Polybrene until only transfected cells remained attached to the culture plate. Additionally, HCMEC/D3 cells were incubated with lentiviral particles containing copGFP using a MOI of 1 overnight. The cells were then washed and incubated in EGM-2 and exposed to 10 mg/mL puromycin until ~90% of adhered cells expressed GFP. Transfected cells were then cultured and used for experiments as needed.

3.1.2. Barrier integrity assessment.

3.1.2.1. Immunocytochemistry. Four vessels were fabricated using the previously described method. After two days in static culture following cell-seeding, the vessels were either left in static conditions or perfused for 24 hours. Upon completion of the experiment, vessels were fixed in 4% paraformaldehyde (Alfa Aesar) for 30 min at room temperature. Following fixation, the top layer of the microfluidic device was separated using a razor blade, and the hydrogel was then removed from the device. Immunolabeling was then performed after blocking in 3% BSA for 30 minutes at room temperature and incubating overnight at 4 C in a primary antibody for either zonula occludin-1 (ZO1) (1:250, Cell Signaling Technology, Product 8193), claudin-5 (1:250, Invitrogen, Product 35-2500), occludin (1:250 Invitrogen, Product 71-1500), glial fibrillary acidic protein (GFAP)

18

(1:100, Santa Cruz, Product sc-166481), or alpha smooth muscle cell actin (1:100, ThermoFisher, Product 41-9760-80). Gels were then washed three times with PBS for 5 minutes and incubated in the appropriate secondary antibody (1:500, Santa Cruz, assorted), 1:500 Hoechst (Sigma), and FITC-phalloidin (Life Tech, F432) for 1h at 37 C. Confocal stacks were acquired using a Nikon A-1 confocal scanning microscope.

3.1.2.2. Permeability testing. Nine vessels were used to quantify the permeability of the vessels following perfusion or static culture. At the completion of the 24-hr experiment, the microfluidic devices were placed on the stage of an inverted epifluorescent (Nikon Ti-E) and perfused with 4 kDa FITC-dextran (Sigma) at a flow rate of 10 µL/min using a linear syringe pump over the span of 10 minutes. This flow rate was chosen to avoid any flow separation and assure fully developed flow throughout the channel and to maintain consistency with previously described permeability assays [15]. Images were taken at 30-s intervals and then imported into ImageJ for analysis. The permeability coefficient was determined using the following equation[96]:

$$P = \frac{di}{dt}\frac{r}{2l_0} \tag{2}$$

Where $\frac{di}{dt}$ is the change in florescent intensity of the region of interest outside the lumen, r is the lumen radius (472 µm) and I_0 is the maximum intensity in the lumen during the test. Permeability was measured at three separate locations corresponding to fully developed flow, near side wall disturbed flow (separated flow), and far side disturbed flow (impingement flow) (designated as I, II, and III).

3.1.2.3. Cell proliferation assays. Three additional vessels were constructed for proliferation assays, which were based in part on a previous study [50]. Briefly, vessels were perfused for 12 hours with EGM-2 using the peristaltic pump and then exposed to 10 μM Bromodeoxyuridine (BrdU) (Alfa Aesar) for the remaining 12 hours. Devices were then briefly washed in PBS and fixed in 4% v/v paraformaldehyde for 30-min at room temperature, quickly washed in PBS, and then permeabilized with 0.2% Triton x100 in PBS for 20 min at room temperature. DNA hydrolysis was performed by removing the hydrogels from the devices and soaking them in a solution consisting of 4 units per mL Turbo DNAse (Thermo fisher) and 0.1 mL DNAse Buffer (Thermo fisher) in PBS for 1 hour at 37C. Gels were washed with PBS then incubated overnight at 4 C with 0.8 μg/mL PE-labeled anti-BrdU (Biolegend) and 1% BSA in PBS. Gels were then counter stained with 1 μg per mL Hoechst for 45 minutes at 37C. In ImageJ, thresholding was used to isolate nuclei prior to using watershedding to isolate individual cells. The ImageJ cell particle counter was used to count the number of nuclei present at three regions of interest in both the disturbed (at the stagnation point) and fully developed regions. In the disturbed region, n = 316-432 Hoechst-positive nuclei were counted. In the fully developed region, n = 261-340 nuclei.

3.1.2.4. Viability assays. Additional vessels were fabricated for viability experiments. Viability was assessed using a Live/Dead kit (Biotium) consisting of calcein AM (2 μM) and ethidium homodimer (4 μM). Vessels were again incubated in static conditions for two days prior to application of flow for 24 hours (controls remained in static conditions for those 24 hours), and then removed from the flow setup, rinsed with PBS, and incubated for 45 minutes in the staining medium prior to imaging. ImageJ was used to

calculate the number of live and dead cells in three different regions for each vessel (three vessels were used for both flow and static conditions).

3.1.2.5. Alignment quantification. Endothelial cell alignment was quantified by transforming the spatial information from the ZO-1 signal into the frequency domain using a fast Fourier transform (FFT) calculated by ImageJ as described in a previous publication [97]. A Gaussian curve was fit to the frequency data, and the half-width of the curve was calculated for cells exposed to fully developed and disturbed flow. This process was repeated for three separate 100 x 100-µm sections from a single immunofluorescence image.

3.1.2.6. Statistical analysis. Pairwise t-tests were used to compare measurements of permeability coefficients and positive BrdU staining. Each comparison was made for sample numbers greater than or equal to 3, and $p < 0.05$ was considered significant. A test for normality was performed using the Shapiro-Wilk test, and $p<0.05$ was considered statistically different from a normal distribution.

3.1.3. Perfusion.

3.1.3.1. Computational fluid dynamics. A computational fluid dynamics (CFD) model was used to predict the flow fields present in the 3D vessels patterned within the microfluidic devices. Prior to the application of flow, brightfield images were acquired of the vessels and used to generate a SolidWorks model that was imported into a commercial finite volume code (Star-CCM+) and discretized by a polyhedral mesh. The maximum flow rate of the peristaltic pump used in our experiments was 4.5 mL/min, so the maximum Reynolds number within the vessels was calculated to be 191. Thus, the flow was laminar

21

in its entirety and there was a sufficient entrance length between Port 1 and the bifurcation to allow for the flow to become fully developed prior to reaching the bifurcation. Furthermore, the Reynolds number necessitated inertial terms in the constitutive flow equation:

$$\rho \, (\vec{V} \cdot \nabla \vec{V}) = -\nabla p + \mu \, \nabla^2 \vec{V}$$

where ρ is the fluid density (kg/m^3), $\vec{V}$ is the fluid velocity vector (m/s), p is the fluid pressure (Pa), and μ is the dynamic viscosity (Pa-s). Additional prism layers were defined in the mesh along the wall boundary to ensure that the near wall effects were adequately resolved. The input flow rate was applied as a velocity boundary condition at Port 1. The gauge pressure at the 20-g needle guide was set to zero, since this provided the outlet for the flow. No-slip boundary conditions were applied at the walls and at Ports 2 and 3 and the 20-g needle guide (locations blocked with silicone grease) to set the velocity to zero at these boundaries. The simulation was run until the solution converged using a steady-state solver.

3.1.3.2.   *Micro-particle image velocimetry flow validation.* Micro-particle image velocimetry (μPIV) was used to validate the CFD model for three independent channels and to characterize the flow regimes present in these channels. Vessels were perfused with steady state flow by a syringe pump (Kent Scientific) at the flow rates determined by the computational model for their individual geometries. These magnitudes ranged from 4 mL/min to 4.5 mL/min. Polyethylene microspheres labeled with Nile Red (Peak excitation: 640nm; mean diameter 1.95 μm; Spherotech Inc.) were suspended 1:500 in PBS containing 0.1% Triton X-100 to prevent bead aggregation and

illuminated and visualized with a dual pulse Nd:YAG laser (125mJ/pulse, 15 Hz, 532 nm; Dantec Dynamics). The pulse width of the lasers was set to 100 ns and the illumination set at a frequency of 0.1 Hz for two seconds (20 individual velocity measurements). Particles were visualized with 10x objective on a Nikon Ti-E inverted microscope, where the focal plane was set to the channel's midpoint. Images were captured using a double-frame CCD camera (FlowSense EO, Dantec Dynamics). Velocity contours were calculated in Dynamic Studio (Dantec Dynamics) using an adaptive PIV algorithm. Velocity contour plots were generated in MATLAB by taking the mean of the 20 velocity measurements. In order to calculate the shear stress at points along the vessel wall, a second order polynomial was fit to the velocity in the boundary layer, and the slope of that function at the wall was calculated.

3.1.3.3. **Design of the pulsatile flow system.** The peristaltic pump system was controlled using an Arduino-based system [98] . A peristaltic motor (Welco) was controlled by an Arduino Uno (Arduino) and a motor board (Ada Fruit). The flow rate magnitude was controlled by using the Arduino to regulate DC voltage powering the motor. A Sensiron flow sensor was used in-line of the perfusion system to monitor the steady flow rate and pulsations. To mimic the arterial pulsation, the pulsatile flow system was designed by superposition of oscillations with the constant mean flow driven by the peristaltic pump. The system included a damper placed in series with the channel, to eliminate the oscillations coming from the peristaltic pump, and a Limnot® linear motor, which was programmed to generate the flow waveform via displacing a 5 mL syringe connected to the actuator system using the LinMot software (open source)[99]. 120mm 12v fans (Corsair)

were mounted to the linear motor to regulate the temperature and prevent the system from overheating.

3.1.3.4. ***3D printing and system assembly.*** The linear actuator along with the 5mL syringe were placed on a 3D printed assembly system to facilitate the movement of the actuator and the syringe while fixing the other components in place. The 3D printed parts were designed using Solidworks then, imported into ultimaker 2+ platform for 3D printing. A total of 5 components (supplemental figure 1) were printed in less than 20 hours. The syringe movement was then facilitated by the placement of linear bearings and rods (McMaster) inside components 1,2 and 3. The system was then mounted to a platform.

3.1.3.5. ***Flow control.*** To apply flow to vessels over a 24-hour timespan, a custom peristaltic pump system was built using an Arduino-based control system. A peristaltic motor (Welco) was controlled by an Arduino Uno (Arduino) and a motor board (Ada Fruit). A Sensiron flow sensor was used in-line of the perfusion system to monitor the applied steady flow rate. System schematics are shown in Supplemental Figure 2. The code to control the pump was written and compiled in Arduino IDE (Arduino) using open source libraries available within the IDE. To minimize pulsations in the system, a dampener was placed in series with the vessel.

3.1.3.6. ***Dynamic mechanical testing.*** Hydrogels with and without astrocytes were polymerized within the central reservoir of the microfluidic devices, and then removed after two days in static culture and transferred to a compression platen for axial dynamic mechanical testing (EZ-SX, Shiamadzu). Due to the fixed geometry of the microfluidic reservoir, all hydrogels had dimensions of 1-cm width, 1-cm length, and 1.6-mm height. The hydrogels were compressed at a frequency of 0.5 Hz between 0 and 15%

strain in an unconfined configuration. The complex modulus was calculated by the ratio of

the maximum stress and maximum strain. The phase shift between the stress and strain

waveforms was used to determine the loss angle, and consequently the storage and loss

modulus of the hydrogels. Three samples were tested for both cellular and acellular

conditions (six total samples).

3.1.4.   RNA sequencing.

3.1.4.1. *mRNA extraction.* To measure gene expression profiles in the

different flow regimes, channels were removed from the microfluidic devices after 24

hours of flow and sectioned into disturbed, impinged, and fully developed regions based

on their geometry using a razor. For each region, the endothelial cell layer was separated

from the rest of the gel prior to RNA extraction. Two channels for each condition were

required to produce a sufficient quantity and quality (RIN > 6.0) of mRNA. The mRNA

was extracted using the PicoPure isolation kit. Twenty-one total channels were required

for these experiments (three channels in duplicate for both steady and pulsatile flow

besides three channels for static condition as a control). For quantitative and qualitative

analysis, the Nanodrop spectrophotometer was used to measure the RNA concentration

and quality. Quality was indicated by measuring the absorbance ratios (260/280). Ratios

around 1.8 were classified as pure and therefore acceptable for gene sequencing.

3.1.4.2. *Gene sequencing and Bioinformatics.* The mRNA was shipped to

an external company (GeneWiz) for next generation Sanger sequencing. To analyze the

sequencing data, a group of open source bioinformatics software programs (FastQC,

Trimmomatic, Htseq, STAR) along with a high-performance computing cluster (16 cores,

60GB) was used to read the sequences and perform a quality control check, trim the bad

reads, align reads to the genome, and count the reads per gene. The disturbed, impinged, and static conditions were compared to the fully developed region as a reference.

3.1.5.   Polymerase chain reaction.

3.1.5.1.   *Astrocyte message level quantification.* After perfusion, hydrogels were removed from the microfluidic device and cut into regions representative of disturbed, impingement, and fully developed regions. mRNA from the astrocytes was isolated using PicoPure RNA Isolation kits (Thermo Scientific) and reverse transcribed to cDNA using qScript (Quantabio). Quantitative PCR was then performed with SYBR Green reagents, with the primers given in Table 1 used to amplify targets. Tests were conducted in triplicate for each region.

Table 2

Primer sequences for astrocyte qRT-PCR

Primer	Forward Sequence	Reverse Sequence
NONO	GTGTAGCGTCGCCGTTACTC	CCTTCATTTTGGCTGCTGGC
VEGF	GACATTGCTGTGCTTTGGGG	AAGGGGAGCAGGAAGAGGAT
HIF1a	TGGCAACCTTGGATTGGATGGA	CCGTCCCTCAACCTCTCAGT
GFAP	CAAAAGCACCAAAGACGGGG	GAGGCTCACTCCCTGTCAAG

Message levels were double normalized to Non-POU domain-containing octamer-binding protein (NONO) from a collagen-only sample. Relative expression was quantified as $2^{-\Delta\Delta C_T}$ where C_T is cycles to threshold. Data are presented as the averaged fold change of collagen/HA gels compared to collagen only gels.

3.1.5.2. *Endothelial cells message level quantification.* After perfusion, hydrogels were removed from the microfluidic device and cut into regions representative of disturbed, impingement, and fully developed regions. mRNA from the endothelial cells was isolated using PicoPure RNA Isolation kits (Thermo Scientific) and reverse transcribed to cDNA using qScript (Quantabio). Quantitative PCR was then performed with SYBR Green reagents, with the primers given in Table 1 used to amplify targets. Tests were conducted in triplicate for each region.

Table 3

Primer sequences for endothelial qRT-PCR

Primer	Forward Sequence	Reverse Sequence
NONO	GTGTAGCGTCGCCGTTACTC	CCTTCATTTTGGCTGCTGGC
Lumican	TCATCCCTGGTTGAGCTGGAT	AGGATAATGGCCCCAGGATCT
MMP1	AAAATTACACGCCAGATTTGCC	GGTGTGACATTACTCCAGAGTTG
MMP3	AGGACAAAGCAGGATCACAGTTG	CCTGGTACCCACGGAACCT
MMP10	TTACATTGCTAGGCGAGATAGG	CAGTCACAGAACATGCAGGAA
MMP12	GATGCTGTCACTACCGTGGGAA	CAATGCCAGATGGCAAGGTTGG

Message levels were double normalized to Non-POU domain-containing octamer-binding protein (NONO) from a collagen-only sample. Relative expression was quantified as $2^{-\Delta\Delta C_T}$ where C_T is cycles to threshold. Data are presented as the averaged fold change of collagen/HA gels compared to collagen only gels.

3.1.5.3. *Statistical analysis.* The open source statistics package, R, was used to perform all statistical analysis. Edge R package was used to determine the differentially expressed genes. To get a sense on how correlated the samples are, a PCA (Principal

component analysis) was performed on the data to reduce the number of columns using the Variance, covariance, covariance matrix, eigenvalues and eigenvectors.

3.1.6. Lumican knockdown.

3.1.6.1. ***Lumican knockdown.*** Lumican knockdown was performed to alter its expression prior to flow experiments, using siRNA transfection with both a target sequence and scrambled sequence for a control. Cells were transfected using the appropriate protocol from Santa Cruz biotechnology. Briefly,cells were plated in a 6-well plate at 200k per well until they reached 60-80% confluency. A mixture of transfection reagent and transfection media was added to the transfection solution, and then to the cells. The transfected cells were incubated at 37 C for 6 hours, then the transfection solution was removed and replaced by EGM-2 for 24 hours prior to seeding.

3.1.6.2. ***Western blot for transfection efficiency.*** Transfection efficiency was verified by western blotting: cells were lysed in sample buffer containing DTT and LDS, boiled, and loaded onto a gel and separated with electrophoresis. Proteins were transferred to a 0.45-µm PVDF membrane. Blots were quantified by measuring band intensity using ImageJ and normalizing relative expression to scrambled conditions. Membranes were incubated with anti-lumican (1:100, Santa Cruz, sc-166871) primary antibodies and visualized with HRP-conjugated secondary antibodies (1:4000, CST L27L9)

3.1.6.3. Permeability testing. Following knockdown validation, twelve channels (n = 6 for knockdown, n = 6 for control) were exposed to steady and pulsatile flow for 24 hours, and permeability experiments were conducted to evaluate the impact of lumican knockdown on barrier integrity by perfusing channels with 4KDa dextran.

29

3.1.6.4. Immunofluorescence. Four vessels were used in this section. Two vessels were perfused for 24 hours, and two others were transfected then perfused for the same period of time. Upon completion of the experiment, vessels were fixed in 4% paraformaldehyde (Alfa Aesar) for 30 min at room temperature. Following fixation, the top layer of the microfluidic device was separated using a razor blade, and the hydrogel was then removed from the device. Immunofluorescence was then performed after blocking in 3% BSA for 30 minutes at room temperature and incubating overnight at 4 C in a primary antibody for zonula occludin-1 (ZO1) (1:250, Cell Signaling Technology, Product 8193).Gels were then washed three times with PBS for 5 minutes and incubated in the appropriate secondary antibody (1:500, Santa Cruz, assorted), 1:500 Hoechst (Sigma), FITC-phalloidin (Life Tech, **F432**) and Lumican conjugated to Alexa 488 (Santa Cruz sc-166871 AF488) for 1h at 37 C. Confocal stacks were acquired using a Nikon A-1 confocal scanning microscope.

3.1.7. Monolayer experiments using flat gels.

3.1.7.1. Cell seeding and flow experiments. For the monolayer experiments, the same hydrogel formulation used in the annulus was polymerized on the treated PDMS coated plates under a sterile 40-mm glass coverslip to create a uniform circular hydrogel to replicate the fully developed flow and 12-mm glass coverslip for disturbed flow. Following removal of the cover slip, HCMEC/d3 were seeded on the gel at a density of 4k/cm2 and allowed to adhere for 30 minutes prior to addition of EGM-2. Monolayers were incubated for 2 days in static culture to ensure confluency, then exposed to fluid shear stress. Fully developed fluid shear stress was applied using a 40-mm 1- degree cone plate on a rheometer (Waters) for 24-hrs on a Peltier plate set to 37oC. Shear stress

gradient was applied using a 40-mm flat plate to mimic the shear stress profiles experienced by disturbed flow. The media was supplemented with HEPES buffer to a final concentration of 10 mM to maintain pH and sterile Millipore was added to the plate during exposure of flow to counteract evaporative loss.

3.1.7.2. *Lumican expression quantification.*

Lumican expression was performed using cell lysates extracted from cell monolayers cultured on the collagen hydrogels exposed to 24hrs of fully developed and disturbed fluid shear stress applied by a cone and plate rheometer. The gels for each condition were removed from the rheometer and washed immediately in ice cold PBS. The gels were then submerged in ice cold lysis buffer (CST) and sonicated. Gels were then spun down at 14,000 g for 5 minutes at 4°C. Supernatants were removed and snap frozen reserving a small aliquot for protein quantification. Samples were equilibrated at 0.5 mg/mL protein concentration using ice cold lysis buffer after thawing in a room temperature water bath. Samples were then loaded on a tris-acetate gel and separated using electrophoresis in tris-acetate buffer. Protein was transferred to a 0.45-µm PVDF membrane. The membrane was incubated overnight with Lumican antibody (1:100) (Santa Cruz, sc-166871) and visualized with HRP-conjugated secondary antibody (1:4000) (CST, L27L9).

3.1.8. Small GTPase activity.

3.1.8.1. *ELISA-based quantification of small GTPase activity*.

To determine the effect of lumican knockdown on small GTPase activity, commercial ELISA kits were purchased from Cytoskeleton (G-LISA) to quantify RhoA activation (Cytoskeleton). For the knockdown and scrambled control, cell lysates were prepared using Cytoskeleton's protocols. Following exposure to flow, vessels were washed with ice cold 1x PBS for 30

seconds. In order to isolate sufficient protein quantity, endothelial cells lysates were prepared from two total vessels for each condition, therefore 100 µL of ice-cold cell lysis buffer with 1x protease inhibitor was injected into each vessel and collected in a microcentrifuge tube. The cell lysate solution was spun at 10,000 g for 1 minute at 4°C to pellet cell debris. The supernatant was collected and snap frozen in liquid nitrogen, reserving a small amount for protein quantification using Precision Red (Cytoskeleton). Prior to measuring GTPase activity, samples were thawed in a room temperature water bath and equilibrated to 0.8 mg/mL for RhoA samples. In order to complete these experiments in triplicate, a total of 12 vessels were fabricated for these studies (Six vessels for each condition).

3.1.9. Lumican mechanics.

3.1.9.1. Fibrillogenesis. Turbidity tests were conducted to assess the microstructure of collagen fibril formation and organization. Collagen fibril formation was measured as previously described[100-102] at 340 nm in a UV sensitive 96-well plate in a plate reader. Each assay consisted of 100 μl of collagen at 20 mg/ml and variable concentrations of recombinant human lumican (VWR) (0.15mg/mL,0.5mg/mL,1.5mg/mL) using distilled water as diluent. All solutions were maintained at 4 °C. Collagen was added to the proteoglycan, mixed by pipetting and reading initiated immediately. Turbidity was measured every 2 min for 60 min. Readings were blanked against the diluent buffer and data were compared to collagen without recombinant lumican as a control. Experimental turbidity curves were analyzed in terms of the maximum rate of turbidity change observed.

3.1.9.2.   Rheology. To determine the impact of lumican on the mechanical properties of the ECM. Recombinant lumican was prepared and added to the collagen gel at different concentrations [102]. Lumican-collagen composite gels was polymerized on a strain-controlled rheometer and the viscoelastic mechanical properties of the gels was assessed as a function of lumican concentrations. Both storage and loss moduli and loss angle were measured for a range of strain magnitude of 0.1% and frequency of 50 Hz, respectively. Data were compared to collagen without recombinant lumican as a control. Each experiment was conducted in triplicates

<h1 style="text-align:center">Chapter IV</h1>
<h1 style="text-align:center">Results</h1>

4.1. Impact of Steady Disturbed Flow on Barrier Integrity

4.1.1. Fabrication and characterization of a 3D in vitro model of a cerebral bifurcation.

A microfluidic device was designed to apply bifurcation flow profiles to a 3D model of a cerebral artery, consisting of an endothelial intima and a smooth-muscle containing media layer surrounded by astrocytes. The device schematic in Figure 3A indicates the location of a 944-μm diameter endothelialized lumen surrounded by a smooth muscle cell-containing annulus with an outer diameter of 1.2 mm in a hydrogel seeded with astrocytes. To induce flow separation, defined as a disruption of a fully developed boundary layer, the flow inlet and cell-seeded vessel were offset by 45 degrees. Figure 3B shows a cross-section at the midpoint of the channel after 3 days in culture, indicating a confluent monolayer of GFP-positive endothelial cells (hCMEC/D3), an annulus of LifeAct-RFP expressing smooth muscle cells (hCMASMC), and an outer hydrogel of glial fibrillary acidic protein (GFAP)-positive astrocytes (NHA). Figure 3C provides a 3D reconstruction of the co-culture vessel, further verifying the stable stratification of the three cell types within the model.
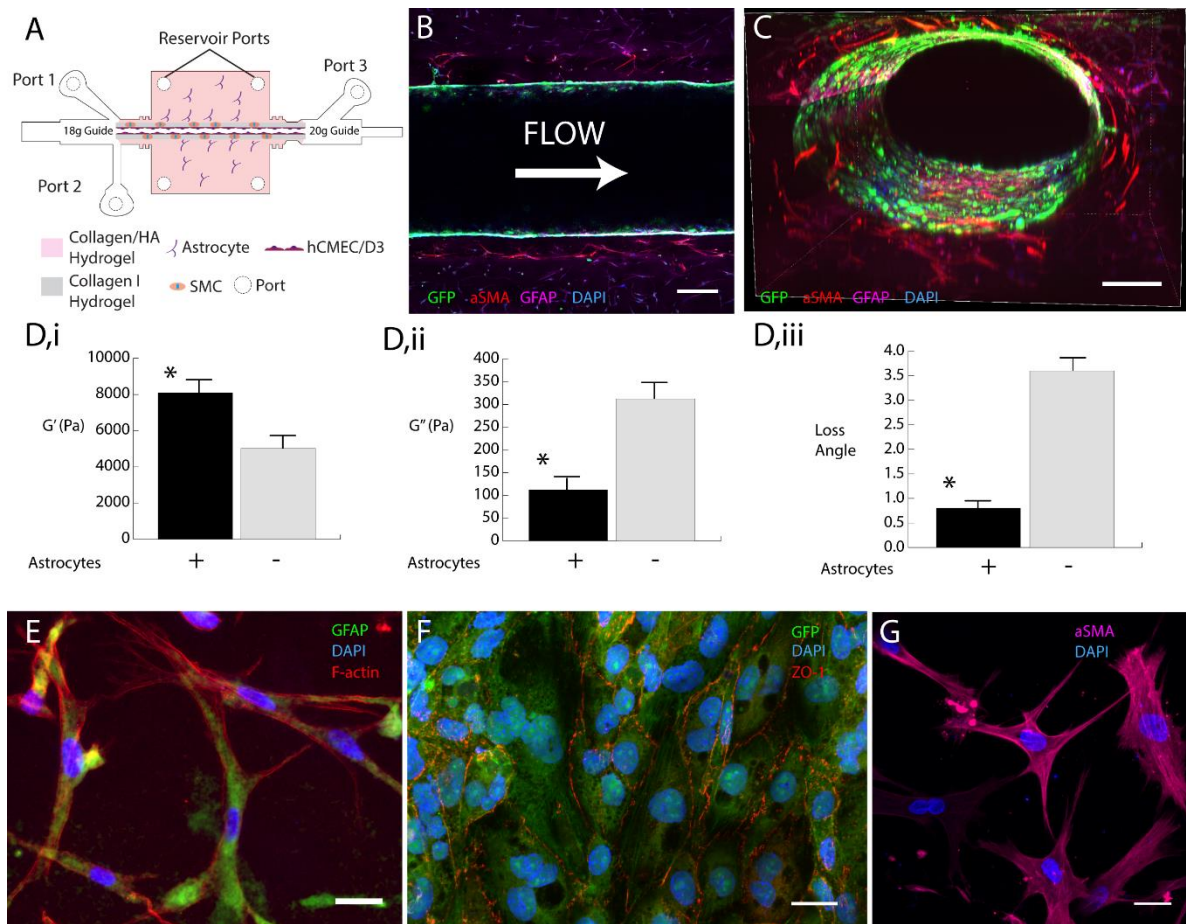
Figure 3. Fabrication of a 3D cerebral bifurcation model. A) Schematic of the microfluidic device showing the location of the ports and the needle guides used to create the layered cell-seeded vessel, B) Cross-section of the vessel at its midpoint with GFP-labelled endothelial cells (green), LifeAct-RFP smooth muscle cells (red), and GFAP-positive astrocytes (magenta). scale = 100 μm. The arrow indicates the flow direction. C) 3D reconstruction of vessel scale = 100 μm. D) Storage moduli (i), loss moduli (ii), and phase angle (iii) of hydrogels seeded with and without astrocytes. (n = 3) E) Astrocytes labeled with DAPI (blue), phalloidin (red), and anti-GFAP (green). F) GFP-labeled endothelial cells (green) exhibiting ZO-1 at cell-cell junctions (red). G) α-SMA-positive smooth muscle cells. Scale bars are 25μm in E, F, and G.

Preliminary flow tests in the microfluidic device revealed that astrocytes were needed within the hydrogel to prevent collapse of channels exposed to high flow rates. Given that previous studies have demonstrated that embedding astrocytes within collagen/hyaluronan composite matrices affects their viscoelastic properties[103], we conducted dynamic mechanical testing of hydrogels with and without astrocytes. The compression testing indicated that hydrogels seeded with astrocytes featured an increased storage modulus (Fig. 3D,i), decreased loss modulus (Fig. 3D,ii), and reduced phase angle (Fig. 3D,iii) compared to acellular controls. This finding is consistent with our previous result that astrocytes alter the mechanical properties of a constrained collagen/hyaluronan hydrogel by exertion of cell-generated forces on the matrix[103]. Hence, astrocytes were required in the model not only to mimic the glial cells surrounding cerebral vasculature in vivo, but also to sustain forces exerted by high Reynolds number flow.

Immunofluorescence analysis using cell type-specific markers verified that the three cell types retained their phenotype after several days in the co-culture. Figure 3E shows the astrocytes within the outer hydrogel: the cells attached to the extracellular matrix and exhibited positive staining for GFAP, a marker of astrocyte activation. Figure 3F provides an image of the confluent endothelial monolayer lining the vessel lumen. After the application of flow, the endothelial cells exhibited localization of zonula occuldin-1 (ZO-1) to the cell-cell junctions, indicative of tight junction formation. Finally, the smooth muscle cells within the annulus maintained their phenotype, as evidenced by positive staining for α-smooth muscle cell actin (α-SMA) (Fig. 3G).

4.1.2. Characterize the steady flow patterns inside the cerebral bifurcation using uPIV and CFD. Disturbed flow was defined by the disruption of a parabolic velocity profile characteristic of fully developed flow and the presence of a recirculation eddy caused by the separated flow. In the computational simulations, the eddy occurred on the near side of the cell-seeded vessel directly downstream of the bifurcation. The location along the wall where the wall shear stress was equal to zero was designated as the stagnation point of the flow. The computational model determined the flow rate that assured the location of the stagnation point was consistent for all geometries, in order to create a reproducible flow field.
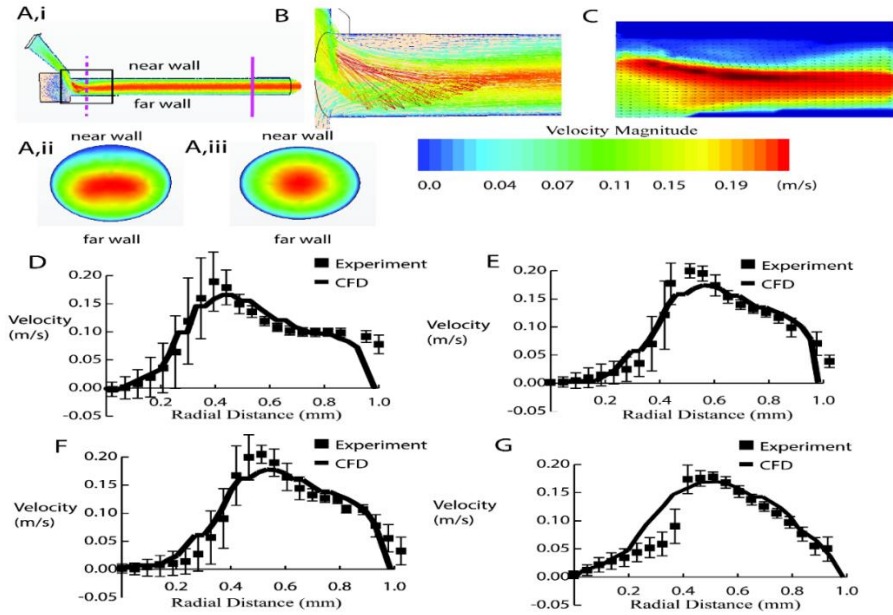
Figure 4. Flow characterization of the bifurcation. A,i) Velocity contour plot generated with the CFD software using a flow rate of 4 mL/min. A,ii) A radial velocity plot in the disturbed region (purple dotted line) and A,iii) fully developed region (purple solid line). B) Velocity contour plot within the boxed region of panel A. C) Velocity contour plot measured with microparticle image velocimetry and processed with a MATLAB code. D) Velocity profile along the channel radius at x= 0.18 mm E) x= 0.33mm, F) x= 0.55mm and, G) x= 1 mm. Error bars indicate the standard deviation between 20 frames.

A 3D computational fluid dynamics (CFD) model was constructed to characterize the flow within the microfluidic device and to determine the flow rate required to cause flow separation along the cell-seeded vessel. A brightfield image of the channel geometry was imported into SolidWorks, discretized, and meshed using a commercial CFD code (Star CCM+). The CFD model predicted flow separation at the near wall of the cell-seeded vessel for an input flow rate of 4 mL/min (Fig. 4A,i). At this location, the velocity profile was no longer parabolic and a recirculation eddy was present. The flow reattached to the wall 2.2-mm downstream of the vessel inlet, as evidenced by the onset of constant wall

shear stress and a fully developed velocity profile. Radial velocity plots in the disturbed (Fig. 4A,ii) and fully developed (Fig. 4A,iii) regions indicated the flow separation caused by the bifurcation. A velocity contour at the bifurcation (Fig. 4B) further exhibited the asymmetric flow profile and separation from the near wall of the cell-seeded vessel.

In order to validate the computational model, microparticle image velocimetry (μPIV) was used to quantify the velocity profile within the vessel. Flow was applied at the 4-mL/min rate used in the computational model, and the velocity contour was measured within the cell-seeded vessel. As Figure 4C indicates, μPIV demonstrated a similar region of separated flow at the inlet of the cell-seeded vessel as the computational model (Fig. 4B). At four distances from the inlet of the cell-seeded vessel (x = 0.28 mm, 0.33 mm, 0.55 mm, and 1 mm), the velocity profiles predicted by the computational model were compared to the measurements from the μPIV measurements (Fig. 4D-G). The plots indicate close agreement between the predicted velocity distributions and those measured by μPIV. For most data points, the computational value falls within one standard deviation of the experimental measurement, with the exception of the contour at x = 1-mm (Fig. 4G) where the computational model overestimates the velocity measured experimentally at radial distances varying from 0.2 to 0.5-mm. A possible cause for this discrepancy is small variations in channel geometry caused by perfusion. To interrogate the effect of perfusion on channel geometry, the deformation of the channel walls was measured during the application of 4.5 mL/min flow and found to increase by 0.5 +/- 0.01% on average along the channel length (measured in three locations for three separate channels). The deformed geometries were then input into the computational model to determine its effect on predicted velocity distribution at x = 1-mm. As Supplemental Figure 3 indicates, changes

to the wall geometry caused by perfusion do not substantially alter the wall shear stress along the channel, suggesting that another factor is likely responsible for the discrepancy in Figure 4G. Nonetheless, the maximum velocity and asymmetry of the distributions were consistent between calculated and experimental data, validating the accuracy of the computational model.
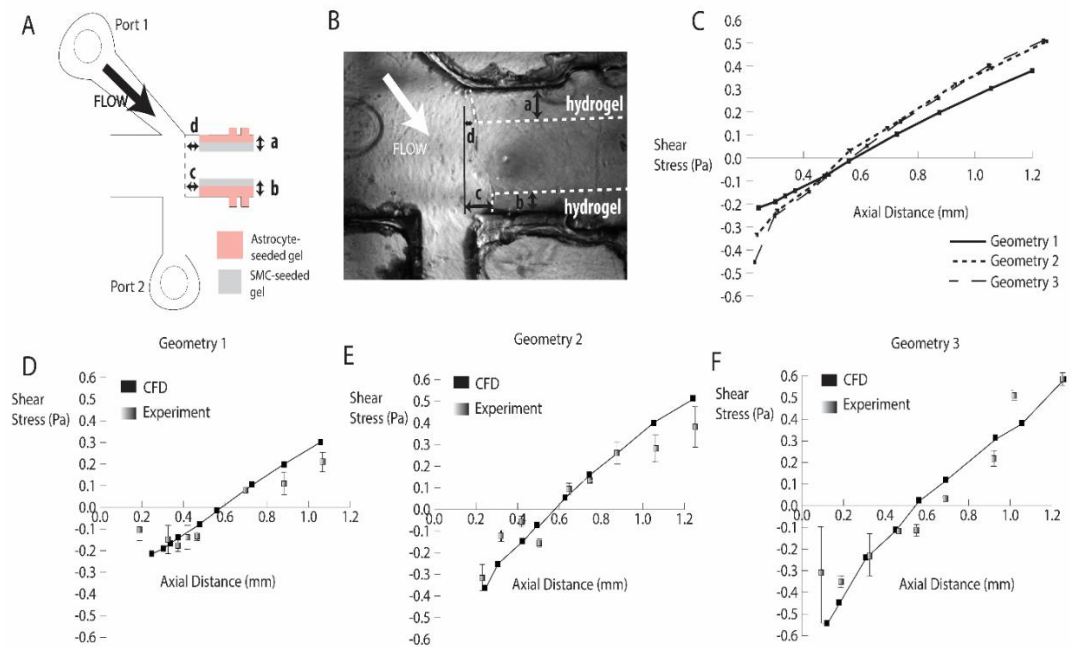
*Figure 5.*Generalized model to account for geometric variation: A) Schematic of the bifurcation detailing the parameters used to quantify differences in vessel geometry. B) A brightfield image indicating the location of these parameters in a sample vessel. C) Wall shear stress profiles generated with CFD for three different geometries and flow rates varying from 4-4.5mL/min. D-F) comparison plots between the experimental and measured wall shear stress (WSS) profiles along a 1.2-mm length of the near wall of the disturbed region for geometries 1,2 and 3. Error bars indicate the standard deviation of 20 measurements.

Having demonstrated the efficacy of the computational model to predict velocity distributions within the device, additional work was conducted to assure that reproducible flow profiles could be applied to multiple channels despite small differences in channel geometry caused by the placement of needles within the hydrogel. Therefore, in order to create a repeatable system for cell studies, an approach was developed to normalize the flow fields for varying geometries. Specifically, the computational model was used to determine the flow rate required to fix the location of the flow stagnation point (where wall shear stress was equal to zero on the near side wall) at the same distance from the inlet regardless of the channel geometry. Four parameters were used to describe the channel geometry prior to application of flow, depicted in Figures 5A and 5B. These parameters provided insight into the position of the hydrogel within the microfluidic device in order to account for slight differences in the placement and orientation of the cell-seeded vessels. Parameters A and B indicated the extent to which the channel was centered within the device, and Parameters C and D described the lateral placement of the hydrogel. Table 2 summarizes the values of these four parameters for three different channel geometries (Geometry 1, Geometry 2, and Geometry 3).

For the three geometries, the average and standard deviation of the stagnation point was predicted to occur at 0.543 mm +/- 0.029 mm and the length of the disturbed region was 2.17 mm +/- 0.44 mm for flow rates varying from 4 to 4.5 mL/min. The predicted shear profiles along the near-side wall of the vessel are shown in Figure 5C. Due to the changes in flow rate, the average shear stress among the three geometries in the fully developed region downstream of the bifurcation was 0.835 Pa +/- 0.056 Pa, which is consistent with physiological levels for the middle cerebral artery [104]. µPIV was used to

validate the shear stress profiles for the three geometries along a 1.2-mm-length of the channel adjacent to the bifurcation on the near wall (Figs. 5D-F). The plots show close agreement between the predicted shear stress distributions and those measured by μPIV. Importantly, the distributions all indicate substantial recirculation zones and a similar stagnation point for all three geometries. These results verify that the stagnation point of the flow can be fixed regardless of small changes to vessel geometry, allowing for a reproducible flow environment for studying the endothelial response in multiple samples.

4.1.3. Evaluate the impact of flow regimes on the BBB integrity.

4.1.2.1. Effects of disturbed fluid flow on endothelial tight junctions and morphology. Having demonstrated that disturbed flow could reproducibly be applied to the vessels despite inconsistencies in channel geometry, experiments were conducted to assess the effect of disturbed flow on the integrity of tight junctions within the endothelial monolayer. In vitro vessels were either exposed to flow for 24-h with flow rates that caused flow separation at the location of the bifurcation or cultured in static conditions as an additional control. Imaging of the monolayer exposed to static conditions revealed that ZO-1 was not fully localized to cell-cell junctions (Fig. 6A,i-ii). In contrast, endothelial cells exposed to fully developed flow exhibited ZO-1 localization to the cell-cell junctions (Fig. 6B,i-ii). In the disturbed region, images of the endothelium at the stagnation point indicated a disorganized monolayer with substantially less ZO-1 staining at the junctions (Fig. 6C,i-ii). FFT analysis suggested that the cells in the fully developed region were significantly more aligned in the direction of flow than cells in the disturbed region (Fig. 6D-E). To provide further evidence of tight junction formation and disruption in these different regions, vessels were also treated with antibodies for claudin-5 and occludin, two

42

additional markers for the tight junctions that are characteristic of the BBB. These images

are provided in Supplementary Figure 4.
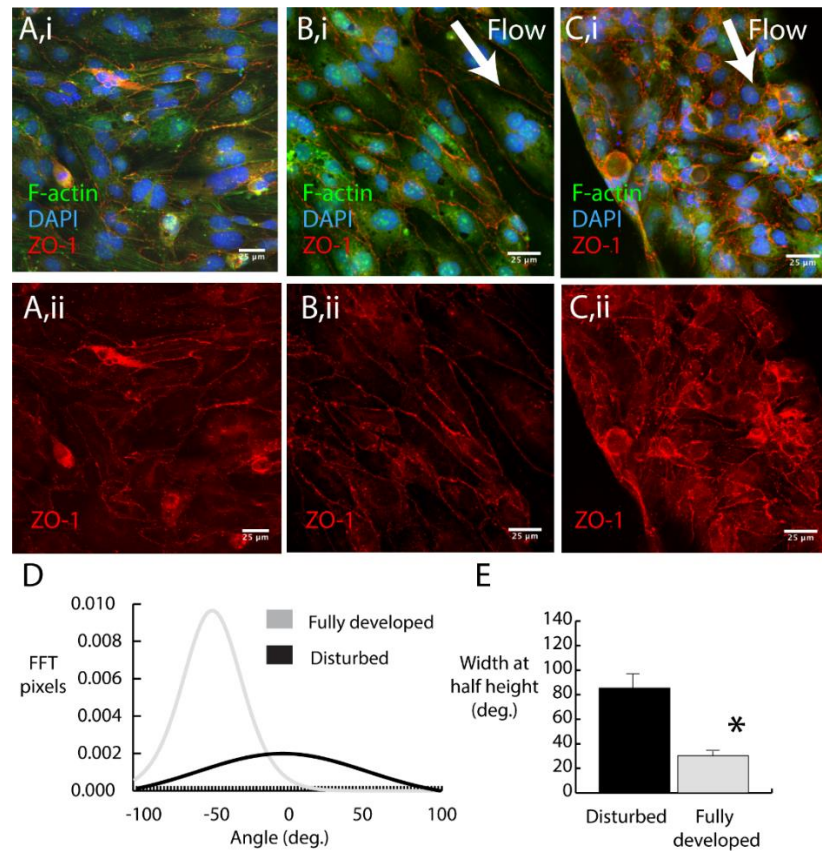
Figure 6. Effects of disturbed flow on endothelial cells tight junctions: A-C) Composite images of ZO-1 (red), DAPI (blue), and phalloidin (green) (i) and with ZO-1 isolated (ii) of the endothelial cells along the near side wall in static conditions (A) and in perfusedchannels at the fully developed (B) and stagnation point of the disturbed region (C). Scale for A-C: 25 μm D) Gaussian distribution of the actin fibers fitted to results of FFT analysis. E) Width at half height of the distributions for disturbed and fully developed regions. * p < 0.05.

4.1.2.2 Effects of disturbed fluid flow on endothelial cell proliferation and

viability. As shown in Figure 7, the endothelium in the disturbed region appeared to have

a higher cell density than the region in the fully developed region downstream of the

bifurcation. To determine whether disturbed flow augmented proliferation in the

disturbed region, a BrdU assay was conducted to compare the number of cells in S-phase

between the disturbed and fully developed regions. Based on channel geometries, flow

rates were chosen to match the wall shear stress distributions used in the

immunofluorescence and permeability assays and applied for 24-h. After 12-h, BrdU was

added into the perfusing medium. Imaging of the fully developed region showed few

BrdU-positive nuclei (Fig. 7A) In contrast, the disturbed region (Fig. 7A) exhibited an

increased number of BrdU-positive nuclei (and higher number of nuclei overall) at the

location of the stagnation point of the near wall (Fig. 7B). Quantification of the disturbed

and fully developed regions indicated a significant increase in the number of BrdU-

positive cells. In the disturbed region: 65% of cells were in S-phase compared to only 3%

in the fully developed region (Fig. 7C). This result is consistent with previous studies that

found increased endothelial proliferation is associated with barrier breakdown [105].

To verify that endothelial cell viability was not affected by the different flow

regimes, a Live/Dead assay was conducted for static,disturbed, and fully developed

conditions. Across all conditions, the viability exceeded 92% regardless of the shear stress

exerted on the endothelium. Furthermore, there were no significant differences in the

number of viable cells between static (Fig. 7D,i), fully developed (Fig. 7D,ii), and disturbed

(Fig. 7D,iii) conditions. Figure 7E provides a summary of the quantified data, indicating

no significant difference in viability between the different flow regimes. These results

44

indicate that although cells in the disturbed region proliferated at a higher rate, they remained viable during the flow experiments.
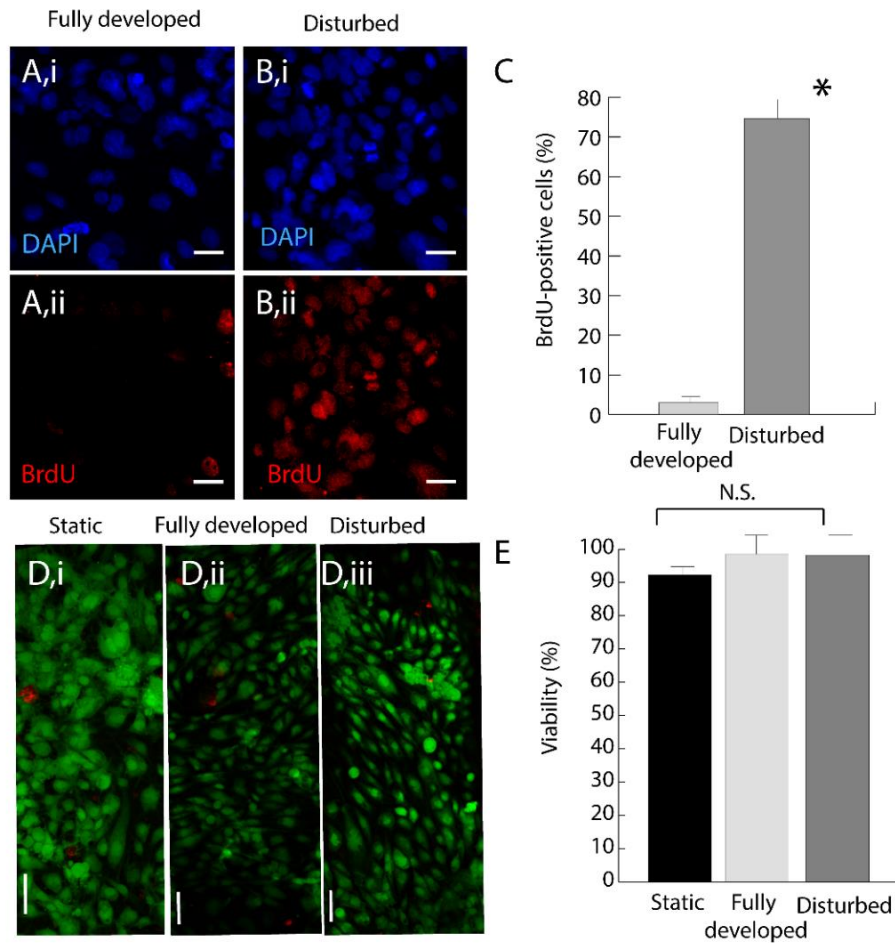
Figure 7. Effects of disturbed flow on endothelial cell proliferation and viability: A-B) DAPI (i) and BrdU (ii) staining of the endothelial lumen for fully developed (A) and disturbed (at the stagnation point of the near wall) (B) regions. Scale bars = 25 m. C) Percent of BrdU-positive nuclei (n=3). *indicates p < 0.05. D) Live (green) / Dead (red) assay for cells exposed to static (i), fully developed (ii), and disturbed (iii) flow. Scale bars = 100 μm. E) Quantification of Live/Dead assay for three different vessels for each condition (n = 3). N.S indicates no significant difference.

4.1.2.2. Quantification of vessel permeability and endothelial-mural/endothelial-glial interaction. Permeability testing provided a quantitative means to assess the integrity of the barrier in response to varying flow regimes. Devices were perfused with dextran to quantify barrier integrity after 24-h of perfusion. The permeability coefficient was measured at the fully developed region downstream of the bifurcation (I) and at the near wall (where flow separates) (II) and far wall (III) adjacent to the bifurcation in the area of disturbed flow. Figure 8A provides an image of a vessel being perfused with dextran to assess barrier permeability and denotes the three regions where the permeability was measured. Figure 8B indicates that the permeability is significantly higher in not only the near wall of the disturbed region (II) compared to the fully developed region (I), but also at the far wall of the disturbed region (III). At this location, the vessel wall experiences impingement flow: the shear stress was elevated compared to other regions of the vessel (1.4 Pa +/- 0.22 Pa) and the shear varied along the axial direction of the vessel. This result supports previous studies linking impingement flow [106] and high shear stress [106] to vascular dysfunction in the brain. In order to verify that the increased dextran transport adjacent to the bifurcation was not due to leakage from the side of the hydrogel, the gradient of fluorescence intensity was graphed in both the axial and radial direction for the disturbed region. Measurements indicate that there is no gradient of fluorescence along the axial direction, indicating that the transport of dextran into the hydrogel originates from the disturbed portion of the cell-seeded vessel. Overall, these permeability tests verify the results of the tight junction staining that suggest disturbed flow disrupts barrier function.
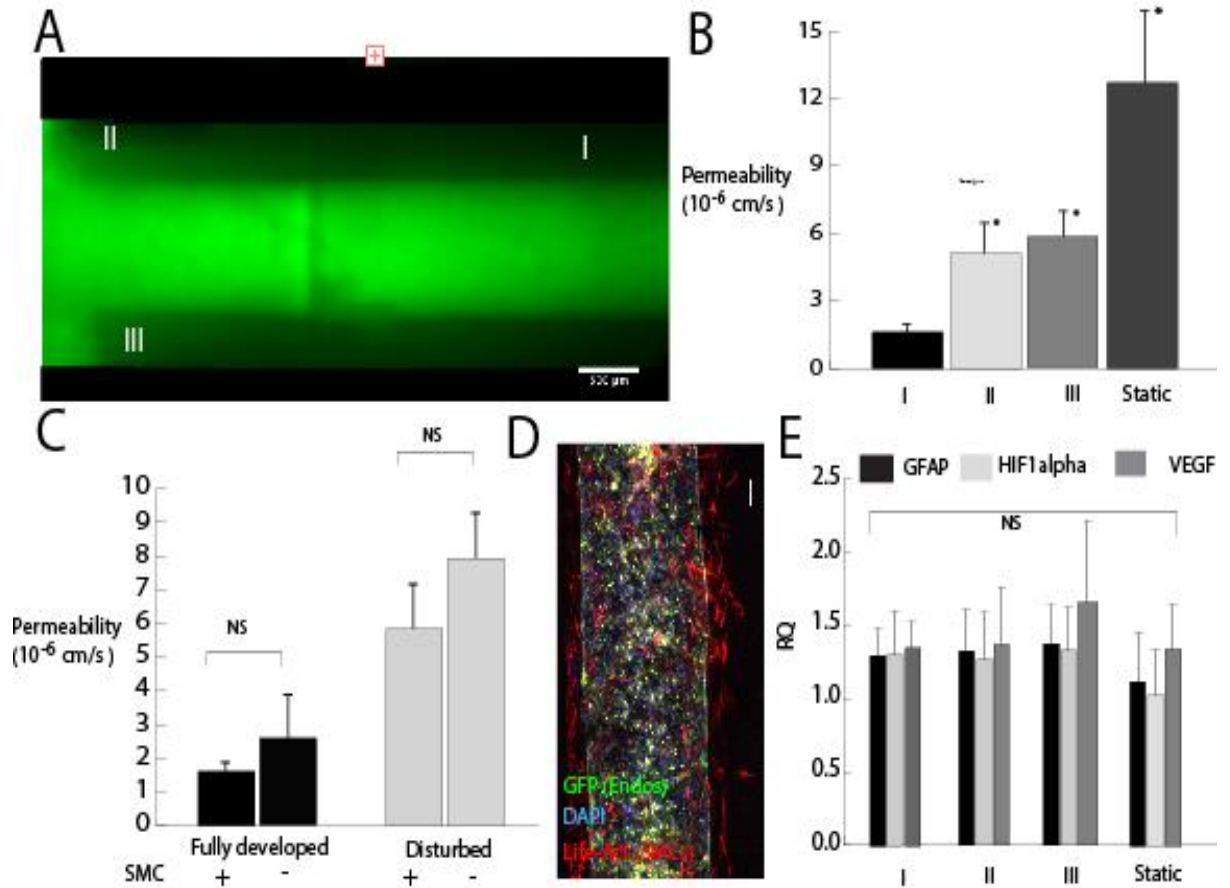
Figure 8. Effect of disturbed flow on vessel permeability and smooth muscle cell and astrocyte interaction. A) An image of dextran perfusion indicating the location of permeability measurements: I) Fully developed, II) Disturbed on the near side wall (separated flow),III) Disturbed on the far side wall (impingement flow). B) Quantification of the permeability constant at these three regions and a static control. (n = 3) C) Quantification of permeability coefficients for vessels lacking smooth muscle cell incorporation. (n = 3) D) A representative image of smooth muscle cell orientation along the endothelialized vessel. E) Relative gene expression of GFAP, HIF1alpha, and VEGF of astrocytes isolated from regions adjacent to endothelial cells exposed to fully developed (I), disturbed (II), impinged flow (III), and static conditions. (n = 3) * indicates $p < 0.05$. N.S indicates no significant difference.

In order to probe endothelial-mural crosstalk, permeability tests were repeated on vessels with smooth muscle cells removed from the annulus. Given the effect of mural cells on regulation of vascular tone[107], lipid absorption[108], and small GTPase signaling within endothelial cells [109], these experiments interrogated whether smooth muscle cells also influenced the response of the BBB to altered shear stress. Figure 8C indicates that the absence of smooth muscle cells did not cause a significant effect in the permeability of the endothelium in the disturbed and fully developed regions. Additional imaging experiments were conducted to determine if the spatial organization of the smooth muscle cells varied along the vessel (Fig. 8D). Quantification of the distance between smooth muscle cell nuclei and the endothelial lumen indicated no significant difference between disturbed and fully developed regions.

Astrocytes in regions adjacent to the three flow regimes (I: fully developed, II: disturbed, and III: impinged) were isolated and lysed following application of flow to determine whether glial cells mediated barrier disruption by undergoing activation or increasing gene expression of paracrine factors known to cause barrier breakdown. Although gene expression does not elucidate the underlying mechanisms regulating the response of astrocytes to their environmental factors, this assay provides insight into whether the flow regime affected the astrocyte cell response. Message level quantification indicated no significant difference in the production of GFAP, which is indicative of glial activation, or in the production of paracrine factors VEGF and HIF1α, which are known to modulate vascular integrity and function. These results verified that astrocytes surrounding the endothelium exposed to different flow regimes did not affect barrier integrity by altering their gene expression.

4.2.   Impact Of Disturbed Pulsatile Flow On The Integrity Of The BBB

4.2.1. Pulsatile flow generation within the 3D bifurcation model. The

perfusion system portrayed in (Fig. 9 A-C) was designed to generate pulsatile, separated

flow waveforms inside a 3D vessel model by superposing oscillations on the constant

mean flow generated by the peristaltic pump. A flow sensor was placed directly

upstream of the channel to measure flow rates (Fig. 9A). The linear actuator was

programmed to recreate the physiological flow waveform depicted in Figure 9D,

exhibiting four inflection points: (1) peak systolic pressure (2) reflected peak; (3)

dicrotic notch, and the (4) following peak [150]. This waveform was applied at a

frequency of 1-Hz to be appropriate for a human cardiac cycle.
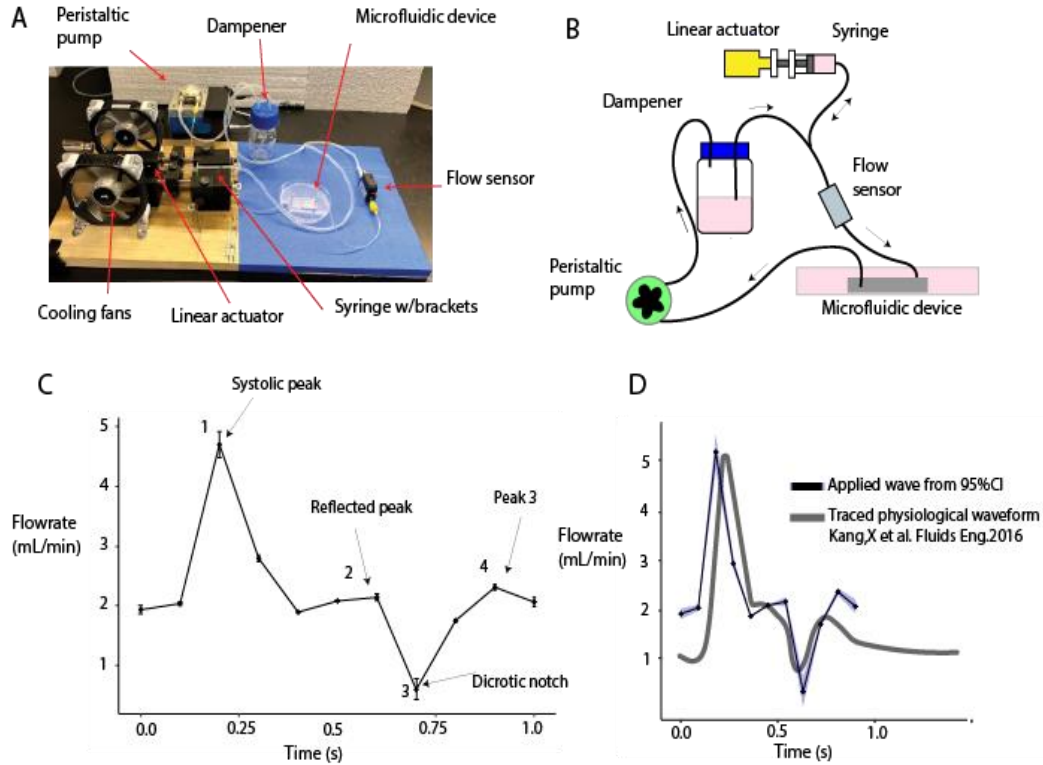
Figure 9. Pulsatile flow system design. A) Photograph of the perfusion system with the peristaltic pump for steady flow generation and the Linmot oscillator for pulsatile superposition. B) Schematic showing the flow circuit used to generate the flow waveform. C) Plot of the physiological-like flow waveform generated with the perfusion system showing the four characteristic points (1) peak systolic pressure; (2) reflected peak, (3) dicrotic notch, and the (4) following peak. Dii) Comparison of the physiological flow waveform and the flow measured in a human carotid artery CCA[7, 110]

4.2.2. Pulsatile flow characterization within the 3D vessel model using μPIV

and CFD. In order to characterize the flow regimes within the 3D vessel model,

brightfield microscopy was used to measure the channel dimensions and orientation

using a previously described method [98]. The geometry was imported into SolidWorks

(Fig. 8A) and then discretized with a polyhedral mesh (Fig. 10Bi,Bii) using a

50

commercial computational fluid dynamics (CFD) code (Star CCM+). The CFD model

predicted separated flow regions at the near wall of the channel at the systolic peak and

the dicrotic and anacrotic notches (Fig. 10C-E), characterized by flow recirculation near

the wall. However, in the diastolic point, no recirculation eddies were present. Overall,

the computational model found a time-dependent velocity changing in direction and

magnitude during the course of the waveform.

Microparticle image velocimetry (µPIV) was used to quantify the time-dependent

velocity profiles within the channel and validate the computational model. Pulsatile flow

was applied to the channel using the same waveform utilized in the CFD model, and the

velocity contour plots were calculated within the channel at the four characteristic time

points (Fig.9D). As Fig. 10C-F indicate, µPIV demonstrated a similar region of separated

flow at the inlet of the channel as the computational model for the points 1,2 and 4.

However, both approaches confirmed there was no backflow measured at the wall. These

results demonstrate that the flow rate is the key parameter governing the flow patterns

within the channel. Therefore, the flow was causing recirculation eddies at high Reynolds

numbers (112, 133 and 306) in the dicrotic notch, the anacrotic notch and the systolic

peak respectively. On the other hand, Reynolds number below 100 (92 at the diastolic

point), was not high enough to cause substantial flow separation and recirculation within

the channel.
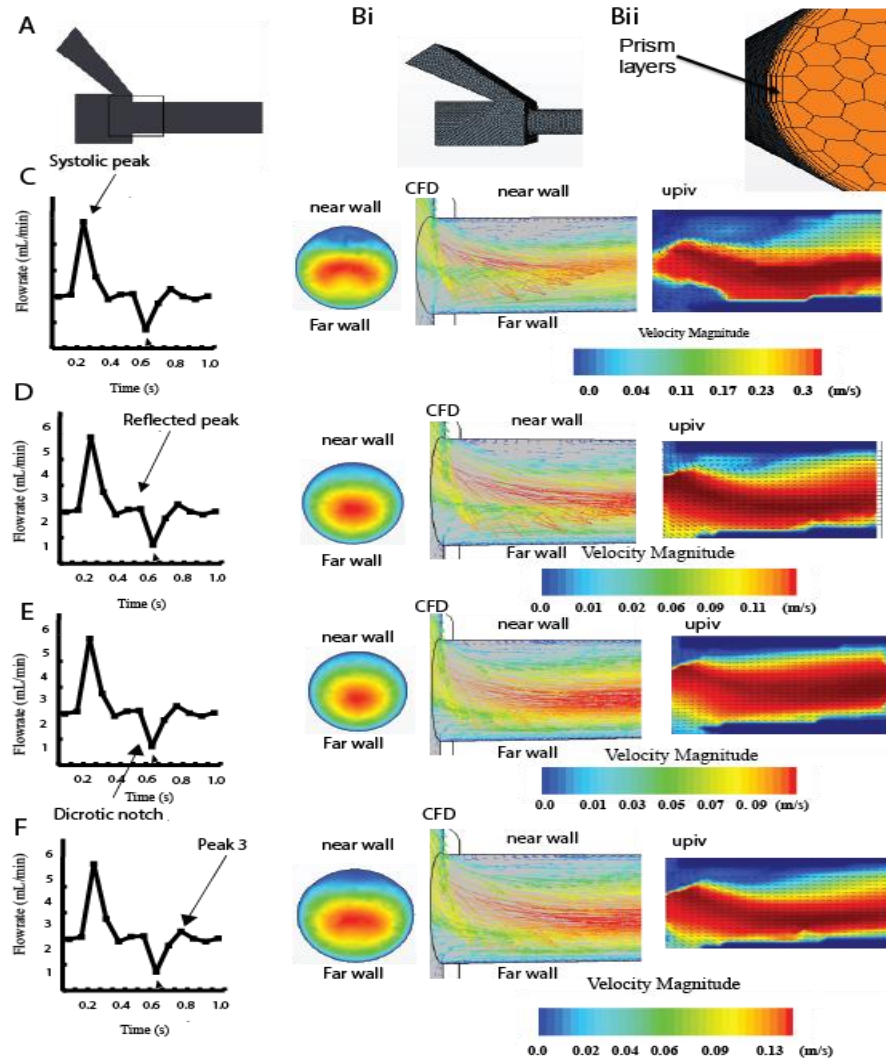
Figure 10. CFD velocity contour plots validated by microPIV along one cycle of the waveform. A) A SolidWorks image of the channel geometry highlighting the hydrogel positioning within the channel, B) Polyhedral mesh generated for the CFD model along with the prism layers along the wall. C) Velocity contour plot at the systolic point generated with the CFD and μPIV, D) Velocity contour plot at the dicrotic notch generated with the CFD and μPIV. E) Velocity contour plot at the diastolic point generated with the CFD and μPIV and, F) Velocity contour plot at the anacrotic notch generated with the CFD and μPIV.

Comparing velocity profiles at three different axial positions provide a means to more quantitatively assess the velocimetry validation of the CFD model. The axial positions include x = 0.2 mm, 0.6 mm, and 1 mm from the inlet of the cell-seeded channel. The plots in Fig. 9 confirm that at a distance of x = 1 mm from the inlet, the flow remained disturbed for the systolic point and the dicrotic and anacrotic notches, evidenced by the lack of a parabolic velocity profile and the negative velocity along the near wall. At the disastolic point, the flow was not fully developed, but the boundary layer on the near wall was not as substantially affected. However, for the diastolic point, while the velocity plot exhibited an asymmetric profile and the flow was not fully developed yet, there was no recirculation at the near wall of the channel, evidenced by the positive velocity values. The radial velocity plots in the flow separation region (Fig.11 A,B,D)) indicated the flow separation caused by the bifurcation in the peak systolic, the diacrotic notch and the anacrotic notch.

For most data points, the computational values fall within one standard deviation of the experimental measurement. While the peak systolic was characterized by minor discrepancies between the experimental and computational results, the maximum velocity and the asymmetry of the profile from both approaches were consistent. Conversely, the velocity comparisons in the diastolic and the dicrotic and anacrotic notches reveal close agreement between the predicted velocity distributions and those measured by µPIV with minimal variations between the 5 µPIV measurements. Overall, these results quantitatively validate the time-dependent velocity profiles predicted by the computational model.
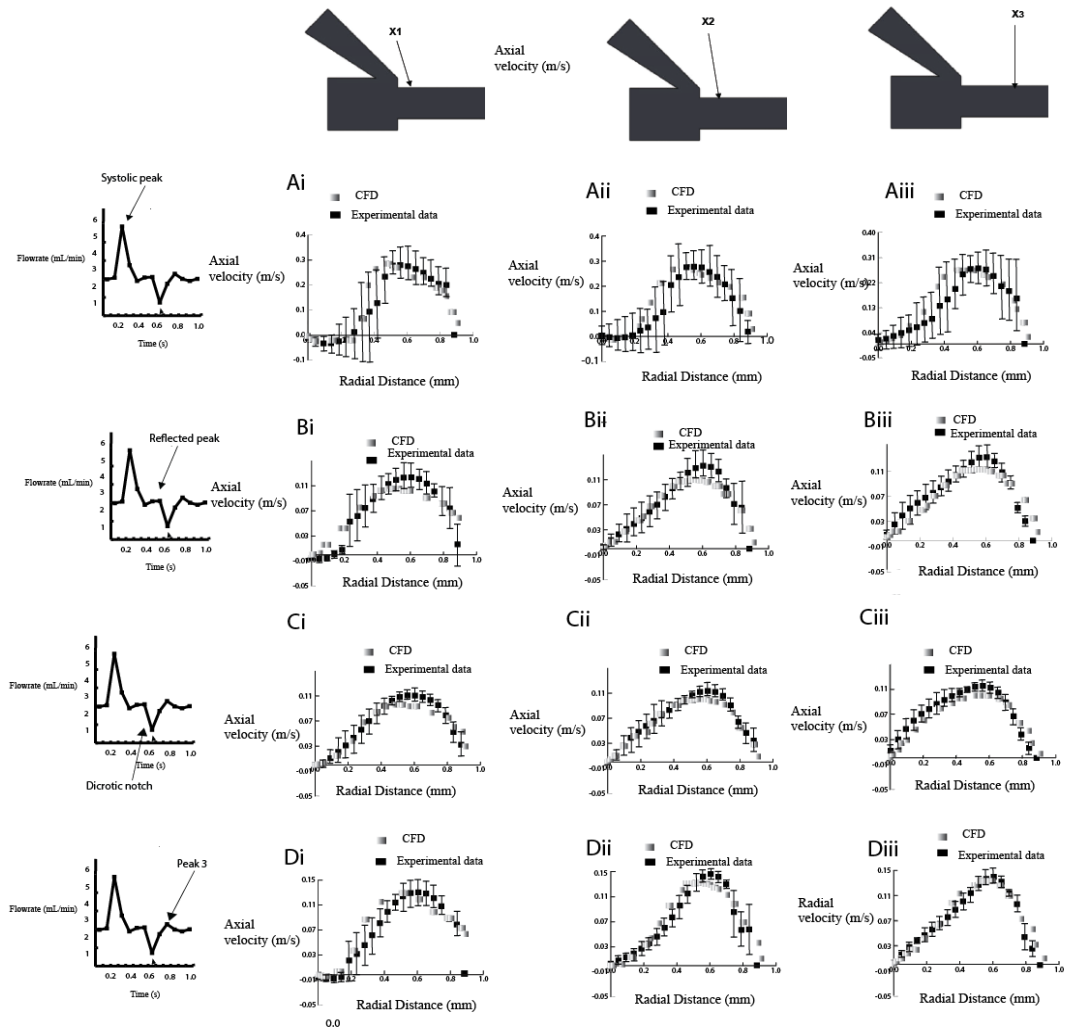
Figure 11. Temporal-spatial matrix of velocity profiles in the bifurcation model., Ai) Velocity profile at the systolic point along the channel radius at x= 0.2 mm Aii) x= 0.6mm, Aiii) and, x= 1mm., Bi) Velocity profile at the dicrotic notch along the channel radius at x= 0.2 mm Bii) x= 0.6mm, Biii) and, x= 1mm. Ci) Velocity profile at the diastolic point along the channel radius at x= 0.2 mm Cii) x= 0.6mm and, Ciii) x= 1mm., Di) Velocity profile at the anacrotic notch along the channel radius at x= 0.2 mm Dii) x= 0.6mm, and Diii) x= 1mm.Error bars indicate the standard deviation between 5 different measurements.

4.2.3. Measurement and validation of wall shear stress profiles along the near wall.

In addition to the velocity profiles, the computational fluid dynamic model (CFD) predicted periodic changes in the instantaneous wall shear stress at different time points of the cycle in the bifurcation model. Furthermore, these periodic changes resulted in varying stagnation points along the channel wall which varied from 0.543 mm for the systolic point (Fig. 12A) to 0.38 mm for the dicrotic and anacrotic notches (Fig. 12B, C). As evidenced by the positive wall shear stress profile in Figure 12.D, no reattachment point was observed in the diastolic flow due to the absence of recirculation at that time point of the waveform. The μPIV validated the wall shear stress profiles along approximately a 1.2-mm-length of the channel adjacent to the bifurcation on the near wall for the four different time points of the flow waveform. The plots showed close agreement between the CFD-predicted wall shear stress profiles and those measured by μPIV, and verified that the systolic, dicrotic and anacrotic notches exhibited recirculation regions at the near wall of the channel. In addition, the spatial and temporal characteristics of the wall shear stress distributions were consistent with the measured velocity profiles.
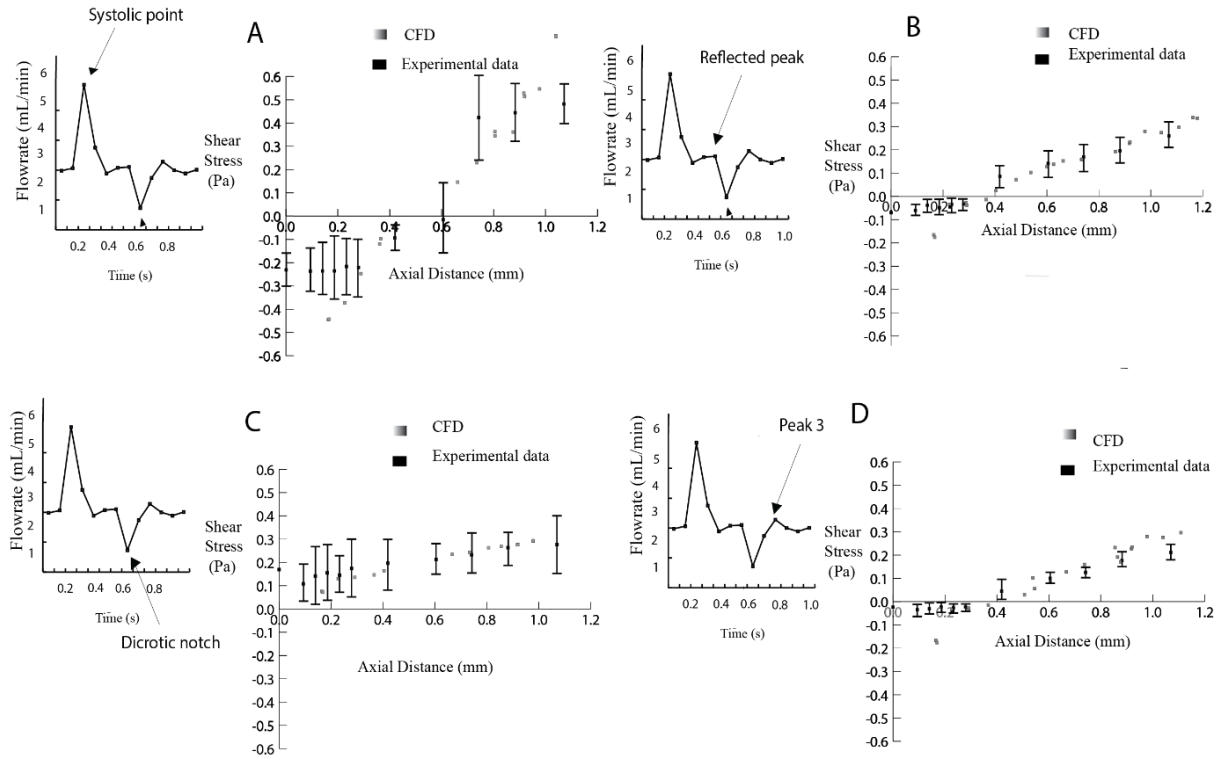
Figure 12. Wall shear stress profiles along the near wall of the bifurcation model A-D) comparison plots between the experimental and measured wall shear stress (WSS) profiles along a 1.2-mm length of the near wall of the disturbed region for the four different time points systolic point, the dicrotic notch, the diastolic point and ,the anacrotic notch in the curve . Error bars indicate the standard deviation of 5 measurements for a duration of 5 seconds.

4.2.3. The impact of pulsatile flow on endothelial cells tight junctions and barrier permeability. Having demonstrated the ability to apply pulsatile flow in the cerebral bifurcation model, channels were perfused with pulsatile flow for 18h to assess the effect of disturbed flow on the integrity of the blood-brain barrier and endothelial cells tight junctions. Confocal images of the vessel revealed that ZO-1 was not fully localized to cell-cell junctions (Fig. 13D-E), in the disturbed region with an increased

stress fiber formation within the cells (Figure 13F). In contrast, endothelial cells exposed

to fully developed flow exhibited ZO-1 localization to the cell-cell junctions (Fig. 13A-

C) and appeared to be aligned to the flow direction. Alignment quantification was

verified by the Fast Fourier Transform (FFT) analysis. Results demonstrated that the cells

in the fully developed region were significantly more aligned in the direction of flow than

cells in the disturbed region (Fig. 13G-H). To determine whether the morphological

changes affected barrier integrity,.permeability tests were performed. Three vessels were

perfused with Dextran after 18 h of pulsatile flow perfusion. The permeability coefficient

measured at the fully developed region was significantly lower than the one measured at

the near wall where the flow separates (Figure 31.I). These results do not contradict our

previous study on the impact of steady disturbed flow on the BBB integrity inside a 3D

cerebral vasculature model. However, a transcriptional analysis is further needed to better

understand the mechanism by which endothelial cells respond to the different natures of

blood flow.
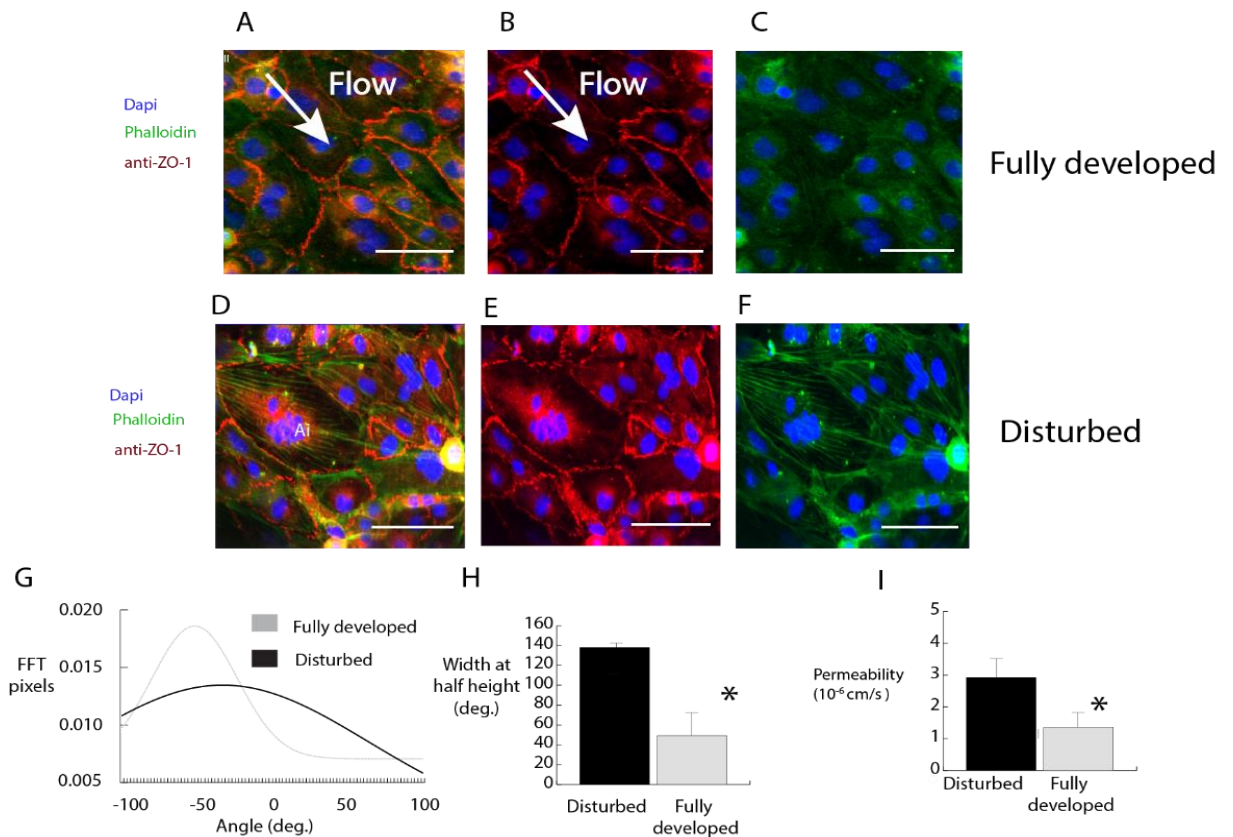
Figure 13. Impact of pulsatile flow on the BBB integrity: A) Composite images of Zo1 staining(red), DAPI (blue) and phalloidin (green) for channels exposed to fully developed flow, B) Zo1 channel isolated for channels exposed to fully developed flow, C) actin channel isolated, D) Composite images of Zo1 staining(red), DAPI (blue) and phalloidin (green) for channels exposed to disturbed flow, E) Zo1 channel isolated for channels exposed to disturbed flow ,F) actin channel isolated, G) FFT pixels , H) width at half height of the distributions for the fully developed and disturbed flow regions and I) Permeability coefficient quantification for the fully developed and disturbed regions. Arrows indicate the direction of flow. Scale bar: 50 um. * p < 0.05.

4.3. RNA Sequencing

4.3.1 General approach. Given the 944-μm diameter of the vessel and a cell density measured to be 182,430 cells/cm^2 +/- 30,230 cell/cm^2 on the near side of the vessel, these studies suggest that 10,000-12,000 cells are exposed to separated flow in

58

each experiment. To verify that this number is sufficient to conduct gene expression analysis, mRNA was extracted from approximately 2-mm long regions of two separate vessels exposed to disturbed,impinged flow, in addition to regions exposed to fully developed flow. With the exception of the static condition, the three flow conditions were derived from the same channels. These isolates exhibited sufficient quality for RNA-sequencing (RIN > 6.0). To analyze the sequencing data, the raw file (Fastq files) were imported in the FASTQC software to check the read quality. All bad reads (not satisfying the Q30 threshhold) were trimmed using the trimmomatic Software. The reads were then aligned to the genome using the STAR software. Finally, HTseq was utilized to assign the aligned reads to genes.

4.3.1. Results.

4.3.1.1. Steady flow results.

4.3.1.1.1. *Principal component analysis*. Differential gene analysis between regions of the vessel exposed to disturbed, fully developed, impinged flow was completed in addition to static conditions as control. To gain a better understanding of the difference in gene expression between these groups, principal component analysis was conducted using the results of RNA sequencing. Results (Figure 14.A) shows that the data clustered in a shear dependent matter for the four different conditions. The static condition is clustered in a region separate from the cells exposed to flow. This analysis is repeated in Figure 14.B focusing on only fully developed and disturbed conditions, again showing the clustering of these two groups. The principal component (PC1) shown in the fully developed – disturbed comparison accounts for 80% of the variation in the data, as plotted in Figure 14.C.
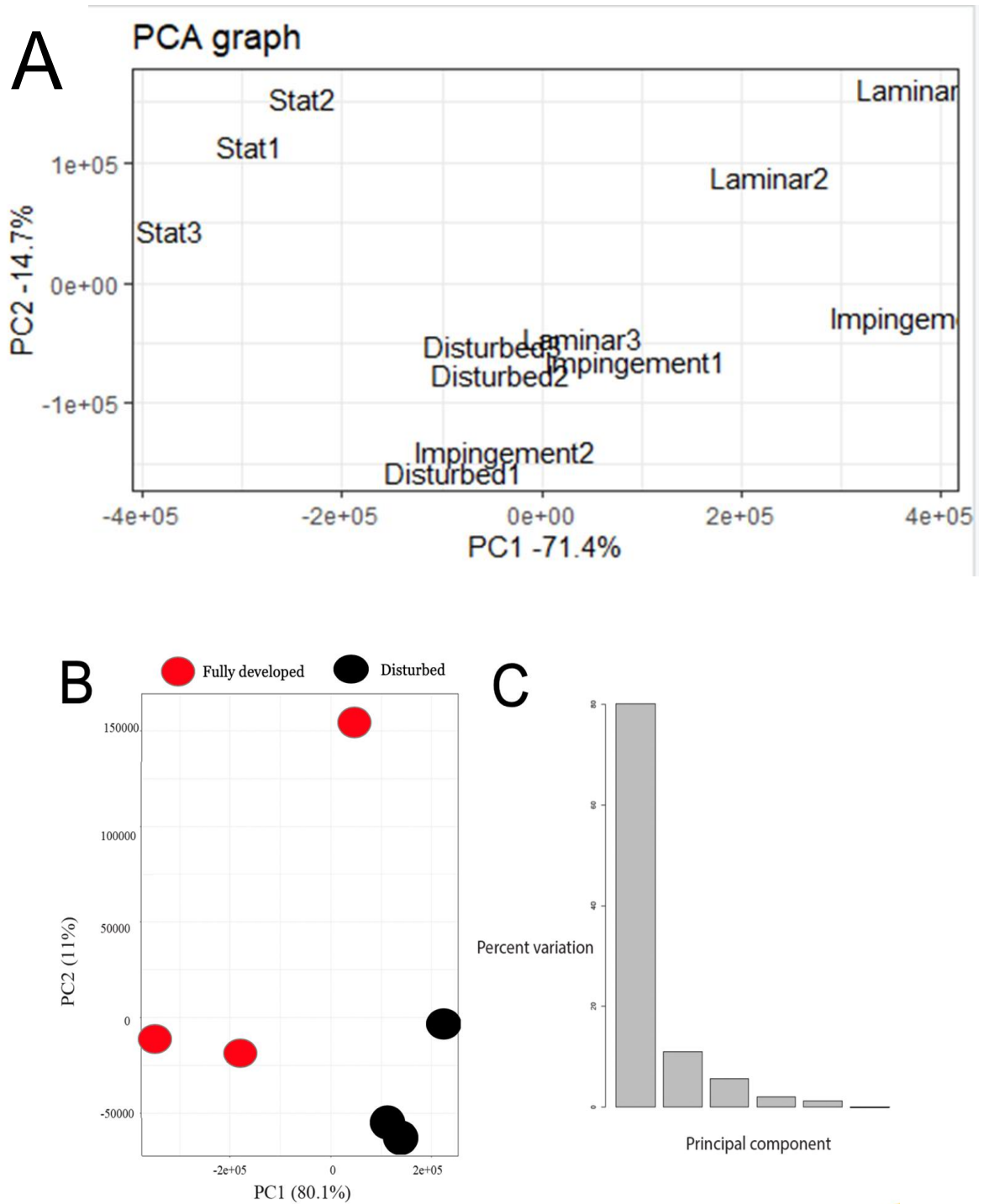
Figure 14. Principal component analysis of the flow conditions. A) plots the data along two components that show separation between the flow groups and static condition, as well as differences between the flow regimes. B) plots focusing on fully developed and disturbed conditions along two components. C) Percent variation plot for the analysis of fully developed and disturbed conditions.

4.3.1.1.2. *Differential gene expression analysis.* The bioinformatics analysis found differences in gene expression between the disturbed and fully developed regions with 645 downregulated and 1040 upregulated genes respectively in the disturbed compared to the fully developed region. The heatmap plot (Fig.15A) shows the 20 most variable genes between the two different regions. Among these genes, the matrix metalloproteinases MMP1, MMP3, MMP12 as well as lumican; a member of the small leucine-rich proteoglycans (SLRPs) were shown to be significantly downregulated in the disturbed region as validated by qrt-PCR (Fig 15.B). Lumican, which has been implicated in ECM organization and collagen fibrillogensesis [111-113], had a 10-fold increase in expression in the fully developed region compared to the disturbed region. Furthermore, lumican expression has been shown to regulate the activation of RhoA through multiple interactions with Rho-GEFs, Rho-GAPs and their effectors in lung cancer [114]. Therefore, these initial studies not only demonstrate the validity of this approach, but also underscore the potential of this model to investigate the effects of disturbed flow on the endothelial cells within the BBB. The heatmap plot (Fig.15A) confirms the differentially expressed genes and shows the 50 most variable genes between the two different regions.
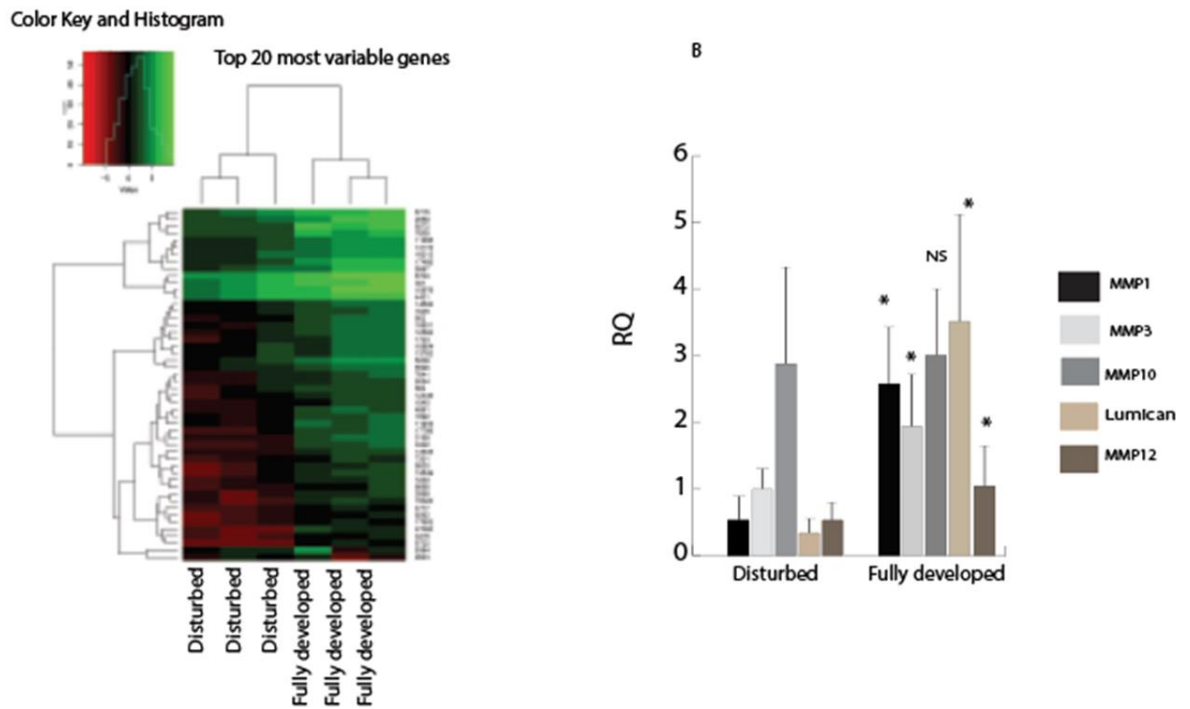
Figure 15. Differential gene expression analysis: A)Heatmap plot showing the difference in expression of genes in the fully developed and disturbed regions using RNA sequencing. B) Message level analysis of five most differentially expressed genes identified usingqrt-PCR for vessels exposed to steady flow.

4.4.   Impact of Lumican Knockdown On The Integrity Of The Barrier In The Endothelium Exposed To Steady Flow

Experiments were conducted to determine whether knocking down lumican in cells exposed to fully developed flow would also cause barrier breakdown, to establish lumican as an important component of barrier formation and maintenance.

4.4.1. Impact of disturbed flow on lumican localization. To further validate

the RNA sequencing results, immunofluorescence was utilized to qualitatively compare

the levels of lumican protein expressed by endothelial cells in the disturbed and fully

developed regions. Figure 16 shows that the lumican expression in the fully developed

region is spread more diffusely throughout the cell, while cells exposed to disturbed flow

exhibited substantially more perinuclear staining. These images also show the difference

in ZO-1 staining between fully developed and disturbed regions, supporting previous

results.
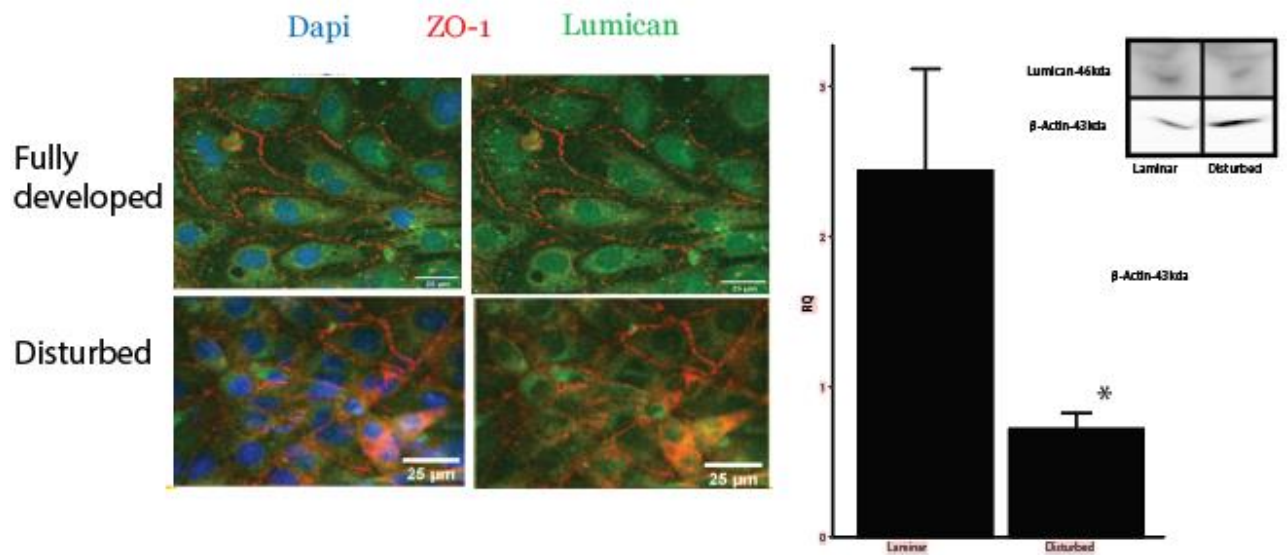
Figure 16. Impact of flow on Lumican expression. A) Immunofluorescence of
endothelial cells in fully developed and disturbed regions. DAPI (blue), anti-ZO-1 (red),
and anti-lumican (green) are shown. The right-side panels remove the DAPI stain to show
the difference in perinuclear staining between conditions. Scale 25um, B) Quantification
of lumican expression in flat gels exposed to fully developed and disturbed flow
conditions using western blot.

To further determine whether the protein expression of lumican mirrors the transcriptional changes, lumican expression by endothelial monolayers exposed to fully developed and disturbed shear stress profiles using a rheometer was quantified using western blot. Results showed that lumican expression in gels exposed to disturbed shear stress profiles is significantly lower than those of fully developed flow further validating that disturbed flow alters the expression of lumican.

4.4.2. Impact of lumican knockdown on the barrier integrity.

4.4.2.1. Lumican knockdown verification. Due to the length of time between when the channel is seeded with endothelial cells and the permeability of the vessel is measured (5 days), the siRNA knockdown efficiency was evaluated at day 5 post-transfection. The knockdown efficiency was verified using western blotting with anti-lumican primary antibodies and HRP-conjugated secondary antibodies. Western blotting validated the effect of gene editing on Lumican expression. Figure 17 shows that the siRNA is approximately 44% efficient in knocking down lumican expression in the endothelial cells, as measured by Western blot.
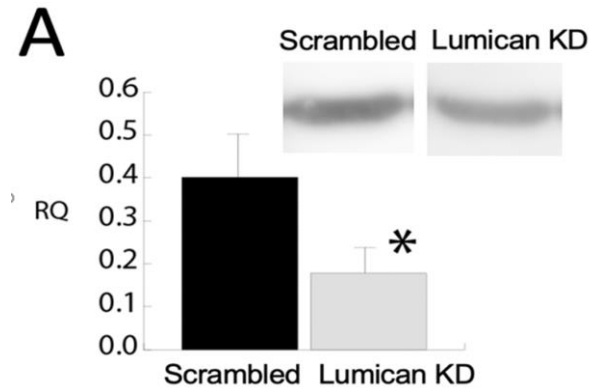
Figure 17. Lumican knockdown studies. A) Validation of knockdown efficiency at day 5 post-transfection.

4.4.2.2. *Impact of lumican knockdown on the barrier integrity under steady and pulsatile flow conditions.*

Two conditions (knockdown and control) were evaluated to determine whether depletion in Lumican impacted he barrier integrity for the steady and pulsatile flow conditions. Immunofluoresence staining showed that the knockdown affected the expression of ZO-1 (red) (green) which was markedly different from the control cells. Vessels treated with scrambled guide sequences were not affected by transfection, ZO-1 is observed at the cell-cell junctions with minimal perinuclear localization. Figure 18.A illustrates the difference in ZO-1 localization to cell-cell junctions in scrambled and knockdown conditions. The knockdown condition resembles the cells exposed to the disturbed flow regimes, indicating substantial barrier breakdown. The immunofluorescence studies were validated by dextran permeability quantification. Knocking down lumican expression drastically altered the barrier response to fully developed flow under steady and pulsatile flow conditions. Figure 18.B finds that using

siRNA to knockdown lumican expression significantly increases the permeability to 4-kDa FITC-labeled dextran. While the permeability of knockdown vessels is not statistically different from vessels exposed to the disturbed flow regimes in the steady flow condition (Fig 18.C), the permeability coefficients for the knockdown and disturbed flow region in the pulsatile flow condition were statistically different (Fig 18.D). Altogether, these results indicate that lumican plays an important role in regulating barrier integrity under steady and pulsatile flow.
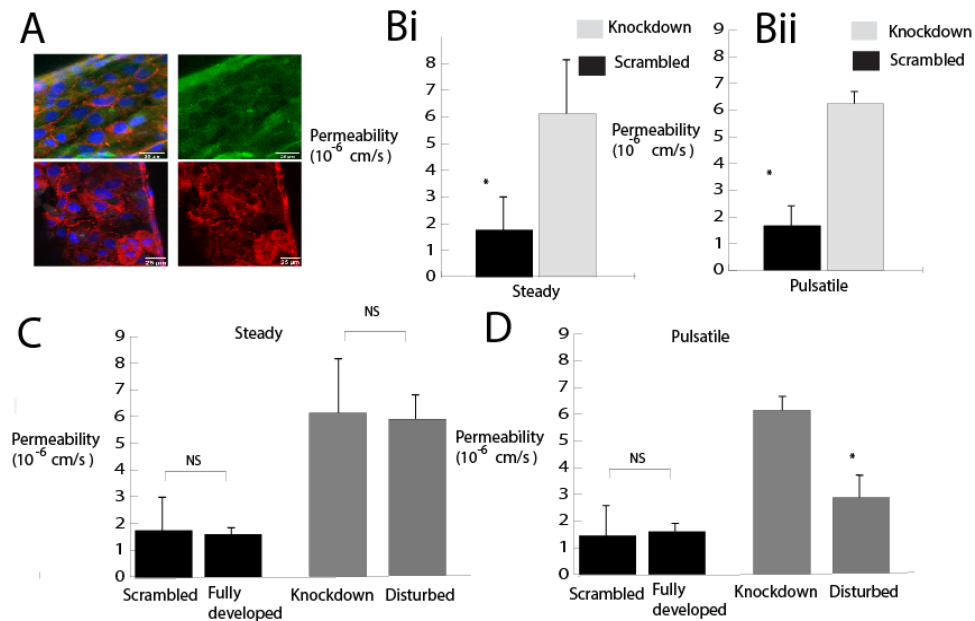
Figure 18. Impact of lumican knockdown on barrier integrity for steady and pulsatile flows A) Immunofluorescence of scrambled and knockdown conditions in the fully developed flow regime. B) Permeability coefficients calculated from 4-kDa FITC dextran for steady flow and pulsatile flow conditions, C) Comparison of permeability coefficients between scrambled control and fully developed flow conditions and knockdown and disturbed conditions for the steady flow, and D) Comparison of permeability coefficients between scrambled control and fully developed flow conditions and knockdown and disturbed conditions for the pulsatile flow.

***4.4.2.3. Impact of lumican knockdown on fluid shear stress
mechanotransduction.*** Previous studies have found that lumican expression alters
Rho/ROCK activity, therefore cells treated with knockdown and scrambled siRNA were
seeded into channels and exposed to flow prior to measurements of barrier integrity.
Studies were conducted to determine the effect of shear stress on RhoA activation within
the 3D BBB model. ELISA assays provided further insight into the effect of flow on the
activation of small GTPases.

Figure 19. Impact of lumican knockdown on RhoA activation.

Figure 19 shows that there is no statistical difference between the knockdown and
scrambled control in the level of RhoA activity, as measured by ELISA assay. Although
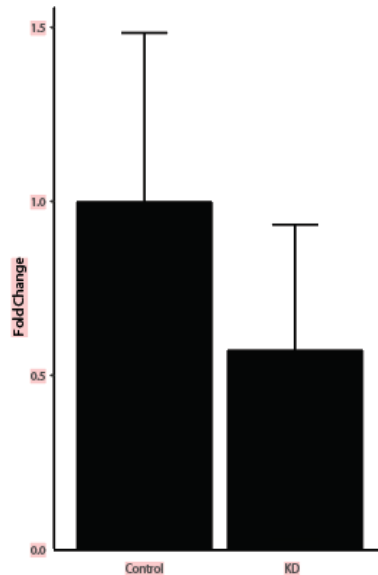lumican has a substantial impact on barrier breakdown, these assays indicate that lumican

does not contribute to changes in RhoA activation suggesting that other specific components of the mechanosensing complex are associated with the blood-brain barrier response to fluid shear stress in the cerebral artery.

4.5. Lumican Mechanics

In order to determine whether lumican alters the mechanics of the surrounding ECM, rheological characterization was conducted to determine whether the presence of the proteoglycan would affect polymerization and viscoelastic properties of a collagen hydrogel.

4.5.1. Turbidity assays and rheology results. The addition of lumican was shown to increase the stiffness of the gel compared to collagen without lumican (Fig. 20A). However, lumican increases the time required for the gel to polymerize in a dose dependent manner, indicating that lumican alters crosslinking process. Fibrillogenesis assays confirmed the effect of the proteoglycan. Initially, the impact of recombinant lumican on collagen fibril formation was measured for three different lumican concentrations (0.01 mg/mL, 0.05mg/mL, and 0.075 mg/mL) (Fig 20.D). Lumican was shown to have an impact on collagen fibrillogenesis compared to the control sample lacking the lumican. Results showed that the addition of lumican increased the time taken before initial fibril formation happened compared to control conditons (collagen only). Therefore, lumican slows down fibrillogenesis with a lower fibril formation plateau. At the end of fibrillogenesis, lumican resulted in overall reduced turbidity indicating a lower fibril diameter compared to the control condition in addition to enhancing collagen fibril stability. These findings suggest that lumican stabilizes the fibril and limits fibril growth which is consistent with previous studies[100]. Therefore, this would reduce rearrangement

68

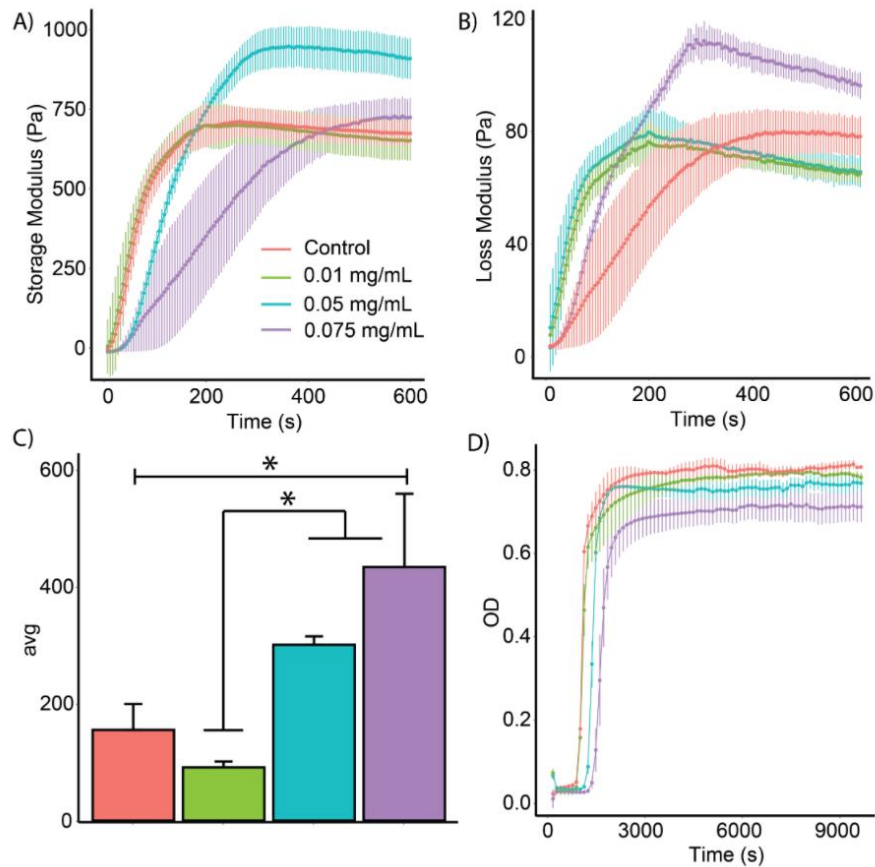of collagen molecules within collagen fibrils in vivo, and reduce heterogeneity of fibril diameter [100].

Figure 20. Impact of lumican proteoglycan on collagen fibrillogenesis and mechanical properties. A) Storage moduus of collagen, and collagen-lumican mixtures, B) Loss modulus of collagen, and collagen-lumican mixtures, C) Impact of lumican on collagen polymerization and , D) Absorbance curve for collagen and collagen-lumican mixtures.

5.1. Disturbed Flow Disrupts The Blood-Brain Barrier In A 3D Bifurcation Model

These results reinforce the growing evidence that fluid shear stress modulates the integrity of the BBB. Whereas a previous study from one of our groups demonstrated the protective effects of low levels of shear on the BBB[15] , here, our findings indicate that shear stress altered by disturbed flow has the opposite effect. Endothelial cells within the region of separated flow exhibit altered morphology, increased permeability, and higher proliferation rates compared to cells in the fully developed flow region downstream of the bifurcation. Although previous studies have identified similar consequences of disturbed flow in other parts of the body[54], the current findings show that vasculature in the brain is also impacted by the altered shear stress exerted by separated flow. Because the barrier function of brain vasculature is more vital than vasculature in other regions of the body due to the inflammation caused by the leakage of plasma components into the brain parenchyma, these results underscore the impact of disturbed blood flow in the brain. Additionally, given that recent studies[115, 116] have found transcellular breakdown precedes the paracellular transport measured here, the effect of disturbed flow on the barrier may be even more pronounced than our experiments indicate.

The results also demonstrate that the cerebral bifurcation model provides a robust platform to study the response of brain vasculature to complex fluid mechanics. Unlike previous in vitro models designed to exert disturbed flow on endothelial cells, the current model preserves the three-dimensionality of the in vivo environment and incorporates both

mural and glial cells in the surrounding hydrogel. Although our results suggest that smooth muscle cells and astrocytes do not modulate the endothelial response to disturbed flow, these findings do not contradict previous findings on the importance of endothelial-mural and endothelial-glial crosstalk. Rather, the results indicate that the endothelium modulates tight junction integrity in response to fluid shear stress independent of other cell types, which is consistent with a previous finding that cerebral endothelial cells exposed to shear stress form tight junctions in the absence of astrocytes[15]. Although the model mimics certain aspects of in vivo vasculature that have yet to be incorporated in vitro, it does not fully recreate the in vivo microenvironment and focuses on a rather short (24-hour) time frame. There are differences in both the ECM content (brain tissue contains minimal fibrillar collagen type I) and a lack of cell types including microglia, pericytes, and macrophages that could affect the specific range and magnitude of shear stress that causes barrier breakdown in vivo. Furthermore, the current microfluidic device exhibits a fixed bifurcation geometry, since the inlet is offset by 45 degrees, and thus cannot mimic the variability present in cerebral bifurcations. Therefore, future work is required to determine whether barrier function is generally reduced adjacent to bifurcations in the brain or additional factors known to exacerbate the effects of disturbed flow in systemic vasculature[24] also exert the same effect on the blood-brain barrier.

However, despite these differences with in vivo vasculature, a particular advantage of this in vitro model is the use of CFD and μPIV to predict and validate the complex flow fields generated in the device. These methods are vital to assuring consistency between the varying channels, since the fabrication of the cell-seeded hydrogels results in small differences in geometries that affect the flow field.

5.2. Impact Of Pulsatile Flow On The BBB

The perfusion system developed here represents a robust, reproducible platform to interrogate the response of cerebral endothelial cells to complex, time-dependent flow fields within 3D protein-based hydrogel microenvironments. Computational fluid dynamics predict a spatial and temporal varying flow field within the channel during application of pulsatile flow, and microparticle image velocimetry validates the model by measuring flow separation at several points within the flow waveform. Both the velocity and wall shear stress profiles demonstrate that disturbed flow patterns exhibit periodic changes in the length of recirculating flow varying from x = 0-mm to approximately 0.55-mm along the near wall of the channel. Endothelial cells within the region of separated flow exhibited altered morphology and tight junctions as well as increased permeability compared to cells in the fully developed flow region downstream of the bifurcation. Overall, these results establish this perfusion system as a means to apply time-dependent, reproducible flow fields to complex vascular geometries, in addition to providing preliminary insight into the effect of pulsatile, disturbed flow on the integrity of the blood-brain barrier,

The perfusion system has sufficient flexibility to mimic a variety of flow waveforms. The waveform used in this study mimics aspects of cerebral blood flow including the systolic and diastolic phases in addition to the inflection points. However, the effect of channel wall compliance can also be assessed in future studies. Intracranial pulsations may play an active role in intracranial fluid dynamics and brain compliance[117]. 3D vessel models combined with the pulsatile perfusion system can be used to investigate the impact of wall compliance on the flow velocity and shear stress profiles. Furthermore,

future studies can also use non-Newtonian fluids to better understand blood flow in complex arterial topologies.

Moreover, the perfusion system can be used to learn more about the mechanobiological response of endothelial cells to complex flow regimes. The results presented here indicate that pulsatile disturbed flow attenuates barrier function compared to fully developed pulsatile flow.

5.3. Establishing A Mechanistic Link Between Disturbed Flow And Aneurysm Formation

RNA sequencing found differences in gene expression between the disturbed and fully developed regions with 645 downregulated and 1040 upregulated genes respectively in the disturbed compared to the fully developed region. Additionally, lumican which has been implicated in ECM organization and collagen fibrillogensesis[111-113], was shown to be significantly upregulated in the fully developed region. Furthermore, the experiments conducted demonstrated that lumican is involved in collagen fibrillogenesis and mediating barrier integrity. The downregulation of the protein is associated with barrier breakdown. However, knocking down lumican has no significant effect on the activity of RhoA. Therefore, the breakdown of the barrier and the reduced expression of lumican are not correlated to increased RhoA activation, suggesting that other mechanisms are involved.

5.4. Future Work

These results are the first to identify lumican as a potential mediator of cerebral aneurysm formation and are therefore a starting point for translational studies that interrogate the proteoglycan as both a therapeutic target and diagnostic candidate. Previous

work in abdominal aneurysms have investigated using lumican levels to diagnose patients at risk for developing such aneurysms. Our results suggest that future studies can interrogate whether lumican is also a marker for cerebral aneurysms. Moreover, these results indicate that lumican is an important mediator of extracellular matrix mechanics. This finding can form the basis of future biophysics studies to determine how proteoglycans modify the properties of viscoelastic substrates, and use this knowledge to advance tissue engineering and regenerative medicine applications in order to increase the clinical impact of this work.

References

1.   Cucullo L, Hossain M, Puvenna V, et al. The role of shear stress in Blood-Brain Barrier endothelial physiology. *BMC Neurosci* 2011; 12: 40. 2011/05/17. DOI: 10.1186/1471-2202-12-40.

2.   Bell RD and Zlokovic BV. Neurovascular mechanisms and blood-brain barrier disorder in Alzheimer's disease. *Acta Neuropathol* 2009; 118: 103-113. 2009/03/26. DOI: 10.1007/s00401-009-0522-3.

3.   Di Marco LY, Venneri A, Farkas E, et al. Vascular dysfunction in the pathogenesis of Alzheimer's disease--A review of endothelium-mediated mechanisms and ensuing vicious circles. *Neurobiol Dis* 2015; 82: 593-606. 2015/08/28. DOI: 10.1016/j.nbd.2015.08.014.

4.   Iadecola C. Neurovascular regulation in the normal brain and in Alzheimer's disease. *Nat Rev Neurosci* 2004; 5: 347-360. 2004/04/22. DOI: 10.1038/nrn1387.

5.   Obermeier B, Daneman R and Ransohoff RM. Development, maintenance and disruption of the blood-brain barrier. *Nat Med* 2013; 19: 1584-1596. 2013/12/07. DOI: 10.1038/nm.3407.

6.   Barakat A and Lieu D. Differential responsiveness of vascular endothelial cells to different types of fluid mechanical shear stress. *Cell Biochem Biophys* 2003; 38: 323-343. 2003/06/10. DOI: 10.1385/cbb:38:3:323.

7.   Jeong JW, Park OK, Park YK, et al. Changes of the carotid artery Doppler flow velocity pattern after sublingual nitroglycerin in patients with hypertension. *Korean J Intern Med* 1998; 13: 22-26. 1998/04/16. DOI: 10.3904/kjim.1998.13.1.22.

8.   Haines N, Wang S, Undar A, et al. Clinical outcomes of pulsatile and non-pulsatile mode of perfusion. *J Extra Corpor Technol* 2009; 41: P26-29. 2009/04/14.

9.   Ku DN, Giddens DP, Zarins CK, et al. Pulsatile flow and atherosclerosis in the human carotid bifurcation. Positive correlation between plaque location and low oscillating shear stress. *Arteriosclerosis* 1985; 5: 293-302. 1985/05/01. DOI: 10.1161/01.atv.5.3.293.

10.   Ornitz DM and Itoh N. The Fibroblast Growth Factor signaling pathway. *Wiley Interdiscip Rev Dev Biol* 2015; 4: 215-266. 2015/03/17. DOI: 10.1002/wdev.176.

11.   Chen F, Ohashi N, Li W, et al. Disruptions of occludin and claudin-5 in brain endothelial cells in vitro and in brains of mice with acute liver failure. *Hepatology* 2009; 50: 1914-1923. 2009/10/13. DOI: 10.1002/hep.23203.

12.   Cristante E, McArthur S, Mauro C, et al. Identification of an essential endogenous regulator of blood-brain barrier integrity, and its pathological and therapeutic implications. *Proc Natl Acad Sci U S A* 2013; 110: 832-841. 2013/01/02. DOI: 10.1073/pnas.1209362110.

13.   van Nieuw Amerongen GP, van Delft S, Vermeer MA, et al. Activation of RhoA by thrombin in endothelial hyperpermeability: role of Rho kinase and protein tyrosine kinases. *Circ Res* 2000; 87: 335-340. 2000/08/19. DOI: 10.1161/01.res.87.4.335.

14.   Iliff JJ, Wang M, Zeppenfeld DM, et al. Cerebral arterial pulsation drives paravascular CSF-interstitial fluid exchange in the murine brain. *J Neurosci* 2013; 33: 18190-18199. 2013/11/15. DOI: 10.1523/JNEUROSCI.1592-13.2013.

15.   Partyka PP, Godsey GA, Galie JR, et al. Mechanical stress regulates transport in a compliant 3D model of the blood-brain barrier. *Biomaterials* 2017; 115: 30-39. 2016/11/26. DOI: 10.1016/j.biomaterials.2016.11.012.

16.   Coloma M, Schaffer JD, Carare RO, et al. Pulsations with reflected boundary waves: a hydrodynamic reverse transport mechanism for perivascular drainage in the brain. *J Math Biol* 2016; 73: 469-490. 2016/01/06. DOI: 10.1007/s00285-015-0960-6.

17.   Weksler BB, Subileau EA, Perriere N, et al. Blood-brain barrier-specific properties of a human adult brain endothelial cell line. *FASEB J* 2005; 19: 1872-1874. 2005/09/06. DOI: 10.1096/fj.04-3458fje.

18.   McLoughlin A, Rochfort KD, McDonnell CJ, et al. Staphylococcus aureus-mediated blood-brain barrier injury: an in vitro human brain microvascular endothelial cell model. *Cell Microbiol* 2017; 19 2016/10/22. DOI: 10.1111/cmi.12664.

19.   Hersom M, Helms HC, Pretzer N, et al. Transferrin receptor expression and role in transendothelial transport of transferrin in cultured brain endothelial monolayers. *Mol Cell Neurosci* 2016; 76: 59-67. 2016/08/29. DOI: 10.1016/j.mcn.2016.08.009.

20.   Masuda H, Shozawa T, Hosoda S, et al. Cytoplasmic microfilaments in endothelial cells of flow loaded canine carotid arteries. *Heart Vessels* 1985; 1: 65-69. 1985/05/01.

21.   Cornhill JF, Herderick EE and Stary HC. Topography of human aortic sudanophilic lesions. *Monogr Atheroscler* 1990; 15: 13-19. 1990/01/01.

22.   Wong AJ, Pollard TD and Herman IM. Actin filament stress fibers in vascular endothelial cells in vivo. *Science* 1983; 219: 867-869. 1983/02/18.

23.   Chappell DC, Varner SE, Nerem RM, et al. Oscillatory shear stress stimulates adhesion molecule expression in cultured human endothelium. *Circ Res* 1998; 82: 532-539. 1998/04/07.

24.   Chiu JJ, Wang DL, Chien S, et al. Effects of disturbed flow on endothelial cells. *J Biomech Eng* 1998; 120: 2-8. 1998/07/24.

25.   DePaola N, Gimbrone MA, Jr., Davies PF, et al. Vascular endothelium responds to fluid shear stress gradients. *Arterioscler Thromb* 1992; 12: 1254-1257. 1992/11/11.

26.   Lei M, Archie JP and Kleinstreuer C. Computational design of a bypass graft that minimizes wall shear stress gradients in the region of the distal anastomosis. *J Vasc Surg* 1997; 25: 637-646. 1997/04/01.

27.   Tardy Y, Resnick N, Nagel T, et al. Shear stress gradients remodel endothelial monolayers in vitro via a cell proliferation-migration-loss cycle. *Arterioscler Thromb Vasc Biol* 1997; 17: 3102-3106. 1997/12/31 23:48.

28.   Davies PF, Shi C, Depaola N, et al. Hemodynamics and the focal origin of atherosclerosis: a spatial approach to endothelial structure, gene expression, and function. *Ann N Y Acad Sci* 2001; 947: 7-16; discussion 16-17. 2002/01/25.

29.   Roy B, Das T, Mishra D, et al. Oscillatory shear stress induced calcium flickers in osteoblast cells. *Integr Biol (Camb)* 2014; 6: 289-299. 2014/01/22. DOI: 10.1039/c3ib40174j.

30.   Seiffert E, Dreier JP, Ivens S, et al. Lasting blood-brain barrier disruption induces epileptic focus in the rat somatosensory cortex. *J Neurosci* 2004; 24: 7829-7836. 2004/09/10. DOI: 10.1523/JNEUROSCI.1751-04.2004.

31.   Robert J, Button EB, Yuen B, et al. Clearance of beta-amyloid is facilitated by apolipoprotein E and circulating high-density lipoproteins in bioengineered human vessels. *Elife* 2017; 6 2017/10/11. DOI: 10.7554/eLife.29595.

32.   Daneman R and Prat A. The blood-brain barrier. *Cold Spring Harb Perspect Biol* 2015; 7: a020412. 2015/01/07. DOI: 10.1101/cshperspect.a020412.

33.   Abbott NJ, Khan EU, Rollinson CM, et al. Drug resistance in epilepsy: the role of the blood-brain barrier. *Novartis Found Symp* 2002; 243: 38-47; discussion 47-53, 180-185. 2002/05/07.

34.   Abbott NJ, Ronnback L and Hansson E. Astrocyte-endothelial interactions at the blood-brain barrier. *Nat Rev Neurosci* 2006; 7: 41-53. 2005/12/24. DOI: 10.1038/nrn1824.

35.   Jiang L, Li S, Zheng J, et al. Recent Progress in Microfluidic Models of the Blood-Brain Barrier. *Micromachines (Basel)* 2019; 10 2019/06/15. DOI: 10.3390/mi10060375.

36.   Shimizu F, Nishihara H and Kanda T. Blood-brain barrier dysfunction in immuno-mediated neurological diseases. *Immunol Med* 2018; 41: 120-128. 2019/04/03. DOI: 10.1080/25785826.2018.1531190.

37.   Sharma G, Sharma AR, Lee SS, et al. Advances in nanocarriers enabled brain targeted drug delivery across blood brain barrier. *Int J Pharm* 2019; 559: 360-372. 2019/02/06. DOI: 10.1016/j.ijpharm.2019.01.056.

38.   Iadecola C. The Neurovascular Unit Coming of Age: A Journey through Neurovascular Coupling in Health and Disease. *Neuron* 2017; 96: 17-42. 2017/09/29. DOI: 10.1016/j.neuron.2017.07.030.

39.   Hallmann R, Horn N, Selg M, et al. Expression and function of laminins in the embryonic and mature vasculature. *Physiol Rev* 2005; 85: 979-1000. 2005/07/01. DOI: 10.1152/physrev.00014.2004.

40.   Patel JP and Frey BN. Disruption in the Blood-Brain Barrier: The Missing Link between Brain and Body Inflammation in Bipolar Disorder? *Neural Plast* 2015; 2015: 708306. 2015/06/16. DOI: 10.1155/2015/708306.

41.   Tsukita S, Furuse M and Itoh M. Multifunctional strands in tight junctions. *Nat Rev Mol Cell Biol* 2001; 2: 285-293. 2001/04/03. DOI: 10.1038/35067088.

42.   Luissint AC, Artus C, Glacial F, et al. Tight junctions at the blood brain barrier: physiological architecture and disease-associated dysregulation. *Fluids Barriers CNS* 2012; 9: 23. 2012/11/13. DOI: 10.1186/2045-8118-9-23.

43.   Cereijido M, Valdes J, Shoshani L, et al. Role of tight junctions in establishing and maintaining cell polarity. *Annu Rev Physiol* 1998; 60: 161-177. 1998/04/29. DOI: 10.1146/annurev.physiol.60.1.161.

44.   Vorbrodt AW and Dobrogowska DH. Molecular anatomy of intercellular junctions in brain endothelial and epithelial barriers: electron microscopist's view. *Brain Res Brain Res Rev* 2003; 42: 221-242. 2003/06/07. DOI: 10.1016/s0165-0173(03)00177-2.

45.   Luissint AC, Federici C, Guillonneau F, et al. Guanine nucleotide-binding protein Galphai2: a new partner of claudin-5 that regulates tight junction integrity in human brain endothelial cells. *J Cereb Blood Flow Metab* 2012; 32: 860-873. 2012/02/16. DOI: 10.1038/jcbfm.2011.202.

46.   Koutsiaris AG, Tachmitzi SV, Batis N, et al. Volume flow and wall shear stress quantification in the human conjunctival capillaries and post-capillary venules in vivo. *Biorheology* 2007; 44: 375-386. 2008/04/11.

47.	Dewey CF, Jr., Bussolari SR, Gimbrone MA, Jr., et al. The dynamic response of vascular endothelial cells to fluid shear stress. *J Biomech Eng* 1981; 103: 177-185. 1981/08/01. DOI: 10.1115/1.3138276.

48.	Colgan OC, Ferguson G, Collins NT, et al. Regulation of bovine brain microvascular endothelial tight junction assembly and barrier function by laminar shear stress. *Am J Physiol Heart Circ Physiol* 2007; 292: H3190-3197. 2007/02/20. DOI: 10.1152/ajpheart.01177.2006.

49.	Siddharthan V, Kim YV, Liu S, et al. Human astrocytes/astrocyte-conditioned medium and shear stress enhance the barrier properties of human brain microvascular endothelial cells. *Brain Res* 2007; 1147: 39-50. 2007/03/21. DOI: 10.1016/j.brainres.2007.02.029.

50.	Chiu J-J and Chien S. Effects of Disturbed Flow on Vascular Endothelium: Pathophysiological Basis and Clinical Perspectives. *Physiological reviews* 2011; 91: 10.1152/physrev.00047.02009. DOI: 10.1152/physrev.00047.2009.

51.	Zhang JH, Badaut J, Tang J, et al. The vascular neural network--a new paradigm in stroke pathophysiology. *Nat Rev Neurol* 2012; 8: 711-716. 2012/10/17. DOI: 10.1038/nrneurol.2012.210.

52.	Dashti R, Hernesniemi J, Niemela M, et al. Microneurosurgical management of middle cerebral artery bifurcation aneurysms. *Surg Neurol* 2007; 67: 441-456. 2007/04/21. DOI: 10.1016/j.surneu.2006.11.056.

53.	Acharya NK, Goldwaser EL, Forsberg MM, et al. Sevoflurane and Isoflurane induce structural changes in brain vascular endothelial cells and increase blood-brain barrier permeability: Possible link to postoperative delirium and cognitive decline. *Brain Res* 2015; 1620: 29-41. 2015/05/12. DOI: 10.1016/j.brainres.2015.04.054.

54.	Zhang XJ, Li CH, Hao WL, et al. Enlarged Anterior Cerebral Artery Bifurcation Angles May Induce Abnormally Enhanced Hemodynamic Stresses to Initiate Aneurysms. *World Neurosurg* 2018; 120: e783-e791. 2018/09/04. DOI: 10.1016/j.wneu.2018.08.167.

55.	Hassan T, Timofeev EV, Saito T, et al. A proposed parent vessel geometry-based categorization of saccular intracranial aneurysms: computational flow dynamics analysis of the risk factors for lesion rupture. *J Neurosurg* 2005; 103: 662-680. 2005/11/04. DOI: 10.3171/jns.2005.103.4.0662.

56.	Levitt MR, Mandrycky C, Abel A, et al. Genetic correlates of wall shear stress in a patient-specific 3D-printed cerebral aneurysm model. *J Neurointerv Surg* 2019; 11: 999-1003. 2019/04/14. DOI: 10.1136/neurintsurg-2018-014669.

57.	Betzer O, Shilo M, Opochinsky R, et al. The effect of nanoparticle size on the ability to cross the blood-brain barrier: an in vivo study. *Nanomedicine (Lond)* 2017; 12: 1533-1546. 2017/06/18. DOI: 10.2217/nnm-2017-0022.

58.	Fede A, Frascaroli D, Vento MG, et al. [Antibiotic prophylaxis of infectious complications of cervico-facial surgery]. *Ann Ital Chir* 1990; 61: 199-202. 1990/03/01.

59.	Gaston JD, Bischel LL, Fitzgerald LA, et al. Gene Expression Changes in Long-Term In Vitro Human Blood-Brain Barrier Models and Their Dependence on a Transwell Scaffold Material. *J Healthc Eng* 2017; 2017: 5740975. 2018/01/11. DOI: 10.1155/2017/5740975.

60.	Hatherell K, Couraud PO, Romero IA, et al. Development of a three-dimensional, all-human in vitro model of the blood-brain barrier using mono-, co-, and tri-cultivation Transwell models. *J Neurosci Methods* 2011; 199: 223-229. 2011/05/26. DOI: 10.1016/j.jneumeth.2011.05.012.

61.	Naik P and Cucullo L. In vitro blood-brain barrier models: current and perspective technologies. *J Pharm Sci* 2012; 101: 1337-1354. 2012/01/04. DOI: 10.1002/jps.23022.

62.	Alcendor DJ, Block FE, 3rd, Cliffel DE, et al. Neurovascular unit on a chip: implications for translational applications. *Stem Cell Res Ther* 2013; 4 Suppl 1: S18. 2014/02/26. DOI: 10.1186/scrt379.

63.	Wilhelm I, Fazakas C and Krizbai IA. In vitro models of the blood-brain barrier. *Acta Neurobiol Exp (Wars)* 2011; 71: 113-128. 2011/04/19.

64.	Grigoryan B, Paulsen SJ, Corbett DC, et al. Multivascular networks and functional intravascular topologies within biocompatible hydrogels. *Science* 2019; 364: 458-464. DOI: 10.1126/science.aav9750.

65.	Griep LM, Wolbers F, de Wagenaar B, et al. BBB on chip: microfluidic platform to mechanically and biochemically modulate blood-brain barrier function. *Biomed Microdevices* 2013; 15: 145-150. 2012/09/08. DOI: 10.1007/s10544-012-9699-7.

66.	Brown JA, Pensabene V, Markov DA, et al. Recreating blood-brain barrier physiology and structure on chip: A novel neurovascular microfluidic bioreactor. *Biomicrofluidics* 2015; 9: 054124. 2015/11/18. DOI: 10.1063/1.4934713.

67.	Herland A, van der Meer AD, FitzGerald EA, et al. Distinct Contributions of Astrocytes and Pericytes to Neuroinflammation Identified in a 3D Human Blood-Brain Barrier on a Chip. *PLoS One* 2016; 11: e0150360. 2016/03/02. DOI: 10.1371/journal.pone.0150360.

68.   Linville RM, DeStefano JG, Sklar MB, et al. Human iPSC-derived blood-brain barrier microvessels: validation of barrier function and endothelial cell behavior. *Biomaterials* 2019; 190-191: 24-37. 2018/11/06. DOI: 10.1016/j.biomaterials.2018.10.023.

69.   Cucullo L, McAllister MS, Kight K, et al. A new dynamic in vitro model for the multidimensional study of astrocyte-endothelial cell interactions at the blood-brain barrier. *Brain Res* 2002; 951: 243-254. 2002/09/25. DOI: 10.1016/s0006-8993(02)03167-0.

70.   Bogorad MI and Searson PC. Real-time imaging and quantitative analysis of doxorubicin transport in a perfusable microvessel platform. *Integr Biol (Camb)* 2016; 8: 976-984. 2016/08/16. DOI: 10.1039/c6ib00082g.

71.   Zheng Y, Chen J, Craven M, et al. In vitro microvessels for the study of angiogenesis and thrombosis. *Proc Natl Acad Sci U S A* 2012; 109: 9342-9347. 2012/05/31. DOI: 10.1073/pnas.1201240109.

72.   Miller JS, Stevens KR, Yang MT, et al. Rapid casting of patterned vascular networks for perfusable engineered three-dimensional tissues. *Nat Mater* 2012; 11: 768-774. 2012/07/04. DOI: 10.1038/nmat3357.

73.   Adriani G, Ma D, Pavesi A, et al. A 3D neurovascular microfluidic model consisting of neurons, astrocytes and cerebral endothelial cells as a blood-brain barrier. *Lab Chip* 2017; 17: 448-459. 2016/12/22. DOI: 10.1039/c6lc00638h.

74.   Henderson JT and Piquette-Miller M. Blood-brain barrier: an impediment to neuropharmaceuticals. *Clin Pharmacol Ther* 2015; 97: 308-313. 2015/02/12. DOI: 10.1002/cpt.77.

75.   Lai CH and Kuo KH. The critical component to establish in vitro BBB model: Pericyte. *Brain Res Brain Res Rev* 2005; 50: 258-265. 2005/10/04. DOI: 10.1016/j.brainresrev.2005.07.004.

76.   Bernas MJ, Cardoso FL, Daley SK, et al. Establishment of primary cultures of human brain microvascular endothelial cells to provide an in vitro cellular model of the blood-brain barrier. *Nat Protoc* 2010; 5: 1265-1272. 2010/07/03. DOI: 10.1038/nprot.2010.76.

77.   Paul G, Ozen I, Christophersen NS, et al. The adult human brain harbors multipotent perivascular mesenchymal stem cells. *PLoS One* 2012; 7: e35577. 2012/04/24. DOI: 10.1371/journal.pone.0035577.

78.   Thomsen LB, Burkhart A and Moos T. A Triple Culture Model of the Blood-Brain Barrier Using Porcine Brain Endothelial cells, Astrocytes and Pericytes. *PLoS One* 2015; 10: e0134765. 2015/08/05. DOI: 10.1371/journal.pone.0134765.

79.   Katyshev V and Dore-Duffy P. Pericyte coculture models to study astrocyte, pericyte, and endothelial cell interactions. *Methods Mol Biol* 2012; 814: 467-481. 2011/12/07. DOI: 10.1007/978-1-61779-452-0_31.

80.   Wang Q, Rager JD, Weinstein K, et al. Evaluation of the MDR-MDCK cell line as a permeability screen for the blood-brain barrier. *Int J Pharm* 2005; 288: 349-359. 2004/12/29. DOI: 10.1016/j.ijpharm.2004.10.007.

81.   Eigenmann DE, Xue G, Kim KS, et al. Comparative study of four immortalized human brain capillary endothelial cell lines, hCMEC/D3, hBMEC, TY10, and BB19, and optimization of culture conditions, for an in vitro blood-brain barrier model for drug permeability studies. *Fluids Barriers CNS* 2013; 10: 33. 2013/11/23. DOI: 10.1186/2045-8118-10-33.

82.   Lippmann ES, Al-Ahmad A, Azarin SM, et al. A retinoic acid-enhanced, multicellular human blood-brain barrier model derived from stem cell sources. *Sci Rep* 2014; 4: 4160. 2014/02/25. DOI: 10.1038/srep04160.

83.   Lippmann ES, Azarin SM, Kay JE, et al. Derivation of blood-brain barrier endothelial cells from human pluripotent stem cells. *Nat Biotechnol* 2012; 30: 783-791. 2012/06/26. DOI: 10.1038/nbt.2247.

84.   Clark PA, Al-Ahmad AJ, Qian T, et al. Analysis of Cancer-Targeting Alkylphosphocholine Analogue Permeability Characteristics Using a Human Induced Pluripotent Stem Cell Blood-Brain Barrier Model. *Mol Pharm* 2016; 13: 3341-3349. 2016/07/17. DOI: 10.1021/acs.molpharmaceut.6b00441.

85.   Helms HC, Abbott NJ, Burek M, et al. In vitro models of the blood-brain barrier: An overview of commonly used brain endothelial cell culture models and guidelines for their use. *J Cereb Blood Flow Metab* 2016; 36: 862-890. 2016/02/13. DOI: 10.1177/0271678X16630991.

86.   Stebbins MJ, Wilson HK, Canfield SG, et al. Differentiation and characterization of human pluripotent stem cell-derived brain microvascular endothelial cells. *Methods* 2016; 101: 93-102. 2015/11/01. DOI: 10.1016/j.ymeth.2015.10.016.

87.   Canfield SG, Stebbins MJ, Morales BS, et al. An isogenic blood-brain barrier model comprising brain endothelial cells, astrocytes, and neurons derived from human induced pluripotent stem cells. *J Neurochem* 2017; 140: 874-888. 2016/12/10. DOI: 10.1111/jnc.13923.

88.   Hollmann EK, Bailey AK, Potharazu AV, et al. Accelerated differentiation of human induced pluripotent stem cells to blood-brain barrier endothelial cells. *Fluids Barriers CNS* 2017; 14: 9. 2017/04/15. DOI: 10.1186/s12987-017-0059-0.

89.   Wang YI, Abaci HE and Shuler ML. Microfluidic blood-brain barrier model provides in vivo-like barrier properties for drug permeability screening. *Biotechnol Bioeng* 2017; 114: 184-194. 2016/07/12. DOI: 10.1002/bit.26045.

90.   Man S, Ubogu EE, Williams KA, et al. Human brain microvascular endothelial cells and umbilical vein endothelial cells differentially facilitate leukocyte recruitment and utilize chemokines for T cell migration. *Clin Dev Immunol* 2008; 2008: 384982. 2008/03/06. DOI: 10.1155/2008/384982.

91.   Andrews AM, Lutton EM, Cannella LA, et al. Characterization of human fetal brain endothelial cells reveals barrier properties suitable for in vitro modeling of the BBB with syngenic co-cultures. *J Cereb Blood Flow Metab* 2018; 38: 888-903. 2017/05/24. DOI: 10.1177/0271678X17708690.

92.   Virgintino D, Errede M, Robertson D, et al. Immunolocalization of tight junction proteins in the adult and developing human brain. *Histochem Cell Biol* 2004; 122: 51-59. 2004/06/29. DOI: 10.1007/s00418-004-0665-1.

93.   Anstrom JA, Thore CR, Moody DM, et al. Immunolocalization of tight junction proteins in blood vessels in human germinal matrix and cortex. *Histochem Cell Biol* 2007; 127: 205-213. 2006/09/08. DOI: 10.1007/s00418-006-0232-z.

94.   Galie PA and Stegemann JP. Simultaneous application of interstitial flow and cyclic mechanical strain to a three-dimensional cell-seeded hydrogel. *Tissue Eng Part C Methods* 2011; 17: 527-536. 2010/12/23. DOI: 10.1089/ten.TEC.2010.0547.

95.   Placone AL, McGuiggan PM, Bergles DE, et al. Human astrocytes develop physiological morphology and remain quiescent in a novel 3D matrix. *Biomaterials* 2015; 42: 134-143. 2014/12/30. DOI: 10.1016/j.biomaterials.2014.11.046.

96.   Adamson RH, Lenz JF and Curry FE. Quantitative laser scanning confocal microscopy on single capillaries: permeability measurement. *Microcirculation* 1994; 1: 251-265. 1994/12/01.

97.   Harris GM, Raitman I and Schwarzbauer JE. Cell-derived decellularized extracellular matrices. *Methods Cell Biol* 2018; 143: 97-114. 2018/01/10. DOI: 10.1016/bs.mcb.2017.08.007.

98.   Bouhrira N, DeOre BJ, Sazer DW, et al. Disturbed flow disrupts the blood-brain barrier in a 3D bifurcation model. *Biofabrication* 2020; 12: 025020. 2019/11/19. DOI: 10.1088/1758-5090/ab5898.

99.   Epshtein M and Korin N. Mapping the Transport Kinetics of Molecules and Particles in Idealized Intracranial Side Aneurysms. *Sci Rep* 2018; 8: 8528. 2018/06/06. DOI: 10.1038/s41598-018-26940-1.

100.   Neame PJ, Kay CJ, McQuillan DJ, et al. Independent modulation of collagen fibrillogenesis by decorin and lumican. *Cell Mol Life Sci* 2000; 57: 859-863. 2000/07/13. DOI: 10.1007/s000180050048.

101.   Rada JA, Cornuet PK and Hassell JR. Regulation of corneal collagen fibrillogenesis in vitro by corneal proteoglycan (lumican and decorin) core proteins. *Exp Eye Res* 1993; 56: 635-648. 1993/06/01. DOI: 10.1006/exer.1993.1081.

102.   Krishnan A, Li X, Kao WY, et al. Lumican, an extracellular matrix proteoglycan, is a novel requisite for hepatic fibrosis. *Lab Invest* 2012; 92: 1712-1725. 2012/09/26. DOI: 10.1038/labinvest.2012.121.

103.   Bowers HC, Fiori ML, Khadela JB, et al. Cell-matrix tension contributes to hypoxia in astrocyte-seeded viscoelastic hydrogels composed of collagen and hyaluronan. *Exp Cell Res* 2019; 376: 49-57. 2019/01/19. DOI: 10.1016/j.yexcr.2019.01.012.

104.   Rossitti S and Stephensen H. Temporal heterogeneity of the blood flow velocity at the middle cerebral artery in the normal human characterized by fractal analysis. *Acta Physiol Scand* 1994; 151: 191-198. 1994/06/01. DOI: 10.1111/j.1748-1716.1994.tb09737.x.

105.   Westin JE, Lindgren HS, Gardi J, et al. Endothelial proliferation and increased blood-brain barrier permeability in the basal ganglia in a rat model of 3,4-dihydroxyphenyl-L-alanine-induced dyskinesia. *J Neurosci* 2006; 26: 9448-9461. 2006/09/15. DOI: 10.1523/JNEUROSCI.0944-06.2006.

106.   Tanweer O, Wilson TA, Metaxa E, et al. A comparative review of the hemodynamics and pathogenesis of cerebral and abdominal aortic aneurysms: lessons to learn from each other. *J Cerebrovasc Endovasc Neurosurg* 2014; 16: 335-349. 2015/01/20. DOI: 10.7461/jcen.2014.16.4.335.

107.   Vanhoutte PM. Endothelium and control of vascular function. State of the Art lecture. *Hypertension* 1989; 13: 658-667. 1989/06/01. DOI: 10.1161/01.hyp.13.6.658.
108.   Minick CR, Stemerman MG and Insull W, Jr. Effect of regenerated endothelium on lipid accumulation in the arterial wall. *Proc Natl Acad Sci U S A* 1977; 74: 1724-1728. 1977/04/01. DOI: 10.1073/pnas.74.4.1724.

109.   Alimperti S, Mirabella T, Bajaj V, et al. Three-dimensional biomimetic vascular model reveals a RhoA, Rac1, and N-cadherin balance in mural cell-endothelial cell-regulated barrier function. *Proc Natl Acad Sci U S A* 2017; 114: 8758-8763. 2017/08/03. DOI: 10.1073/pnas.1618333114.

110.   Holdsworth DW, Norley CJ, Frayne R, et al. Characterization of common carotid artery blood-flow waveforms in normal human subjects. *Physiol Meas* 1999; 20: 219-240. 1999/09/04. DOI: 10.1088/0967-3334/20/3/301.

111. Chakravarti S, Stallings RL, SundarRaj N, et al. Primary structure of human lumican (keratan sulfate proteoglycan) and localization of the gene (LUM) to chromosome 12q21.3-q22. *Genomics* 1995; 27: 481-488. 1995/06/10. DOI: 10.1006/geno.1995.1080.

112. Kao WW, Funderburgh JL, Xia Y, et al. Focus on molecules: lumican. *Exp Eye Res* 2006; 82: 3-4. 2005/10/11. DOI: 10.1016/j.exer.2005.08.012.

113. Ameye L and Young MF. Mice deficient in small leucine-rich proteoglycans: novel in vivo models for osteoporosis, osteoarthritis, Ehlers-Danlos syndrome, muscular dystrophy, and corneal diseases. *Glycobiology* 2002; 12: 107R-116R. 2002/09/06. DOI: 10.1093/glycob/cwf065.

114. Yang C-T, Li J-M, Chu W-K, et al. Downregulation of lumican accelerates lung cancer cell invasion through p120 catenin. *Cell Death & Disease* 2018; 9: 414. DOI: 10.1038/s41419-017-0212-3.

115. De Bock M, Van Haver V, Vandenbroucke RE, et al. Into rather unexplored terrain-transcellular transport across the blood-brain barrier. *Glia* 2016; 64: 1097-1123. 2016/02/09. DOI: 10.1002/glia.22960.

116. Knowland D, Arac A, Sekiguchi KJ, et al. Stepwise recruitment of transcellular and paracellular pathways underlies blood-brain barrier breakdown in stroke. *Neuron* 2014; 82: 603-617. 2014/04/22. DOI: 10.1016/j.neuron.2014.03.003.

117. O'Rourke MF and Hashimoto J. Mechanical factors in arterial aging: a clinical perspective. *J Am Coll Cardiol* 2007; 50: 1-13. 2007/07/03. DOI: 10.1016/j.jacc.2006.12.050.
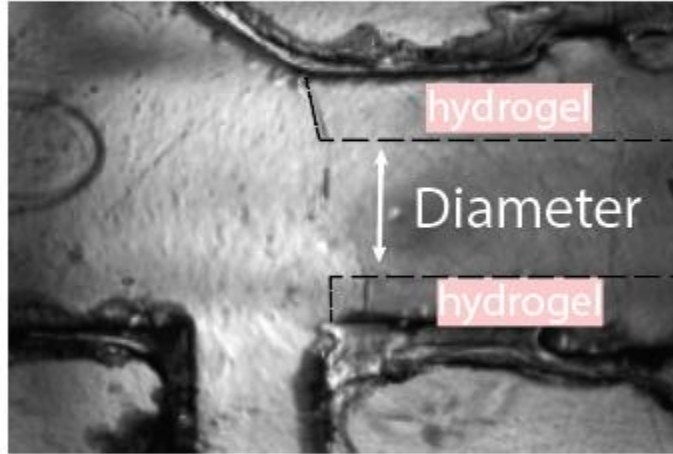
Appendix A

Characterization Of The Channel Geometry

Figure A1. Bright field image of the channel geometry
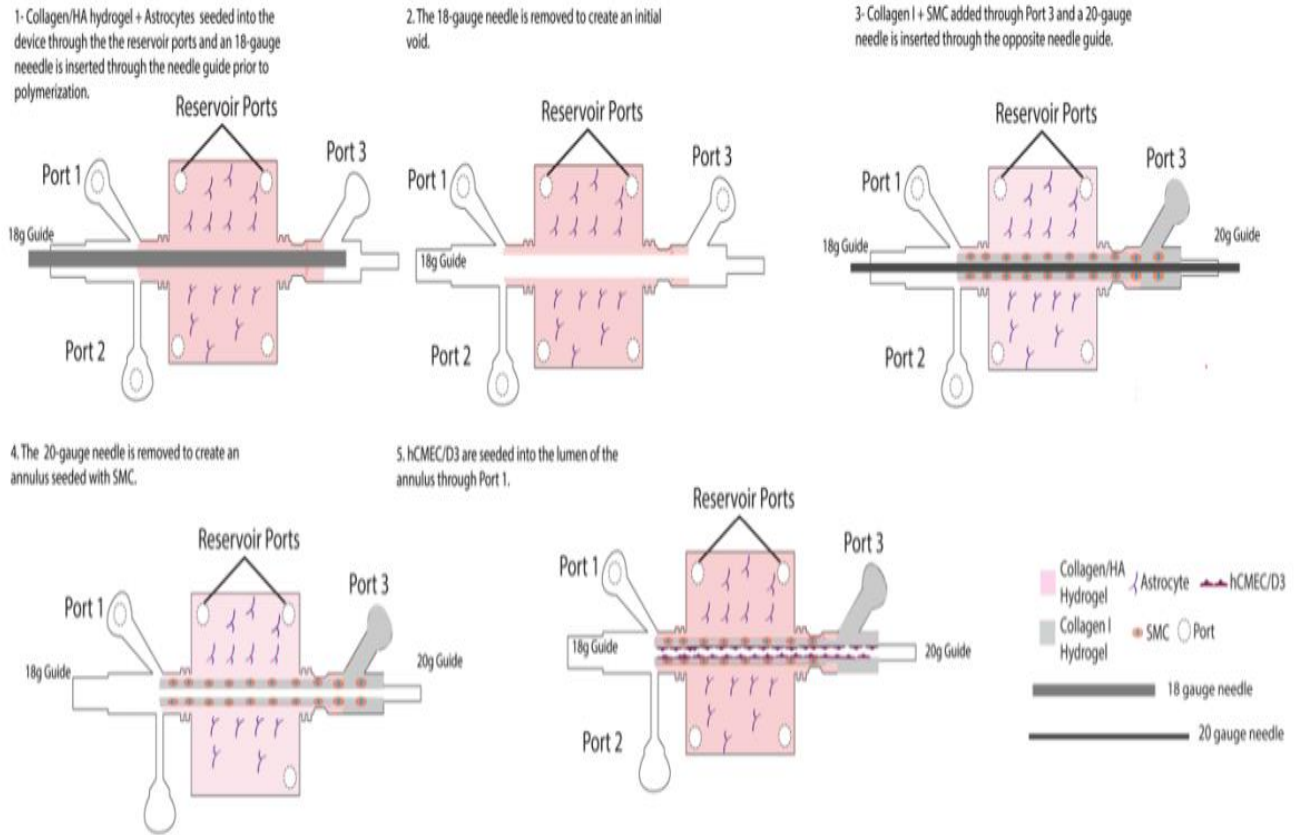
Appendix B

Vessel Fabrication Process

Figure B1. Vessel fabrication process

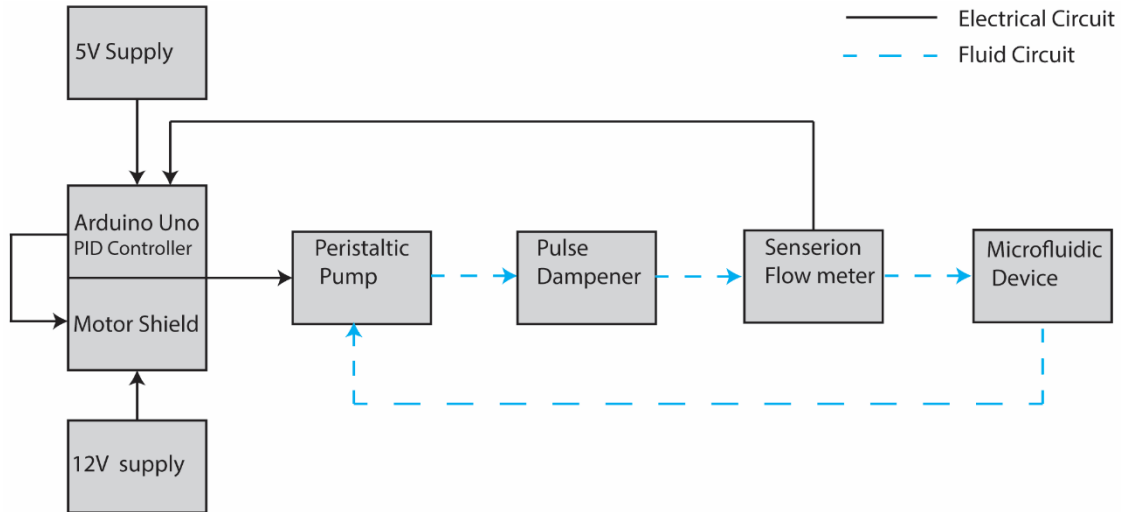**Flow Controller Setup.**

Figure C1. Electrical connections and feedback, along with the flow circuit used to perfuse the devices.

Appendix D
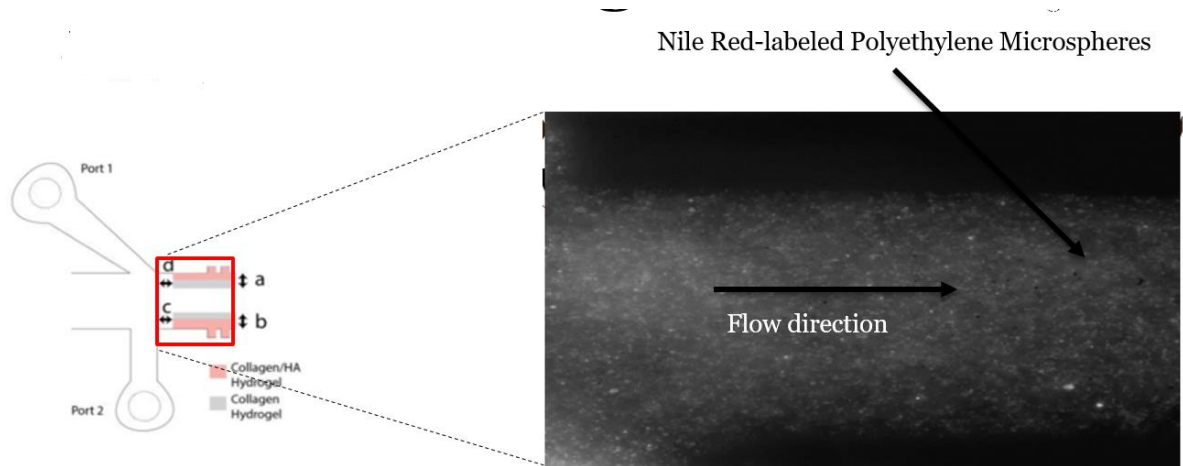
Microparticle Image Velocimetry

Figure D1. Microparticle image velocimetry experiment. The tracer solution was prepared from Nile Red-labeled Polyethylene Microspheres (Peak excitation: 640nm; mean diameter 1.95um; Spherotech Inc.) The beads were illuminated and visualized with a dual pulse laser. The velocity was measured by tracking the beads movement

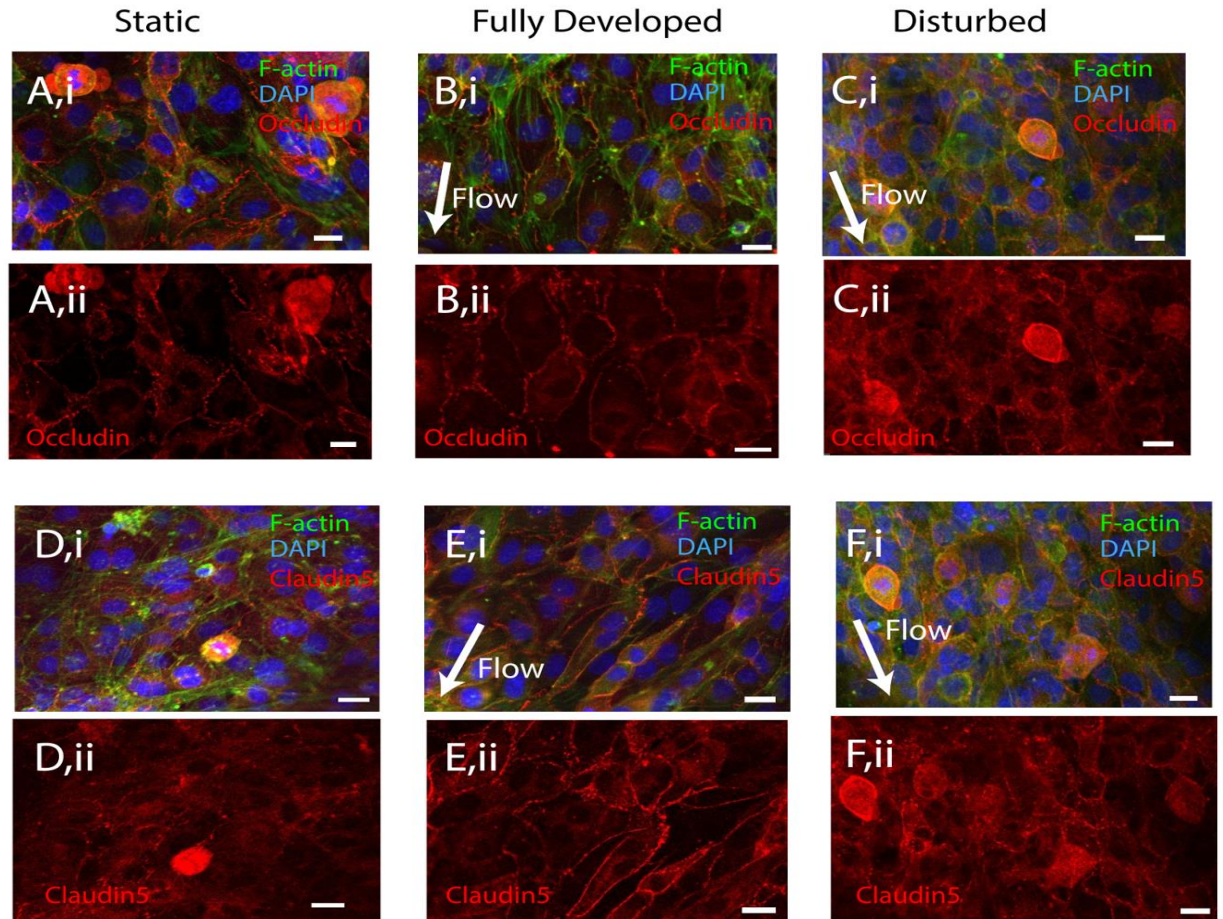## Immunofluorescence Using Claudin-5 And Occluden

Figure E1. Confirmation of tight junction formation and disruption. A-C) Composite images of occludin (red), DAPI (blue), and phalloidin (green) (i) and with occludin isolated (ii) of the endothelial cells along the near side wall in static conditions (A) and in perfused channels at the fully developed (B) and stagnation point of the disturbed region (C). D-F) Composite images of occludin (red), DAPI (blue), and phalloidin (green) (i) and with occludin isolated (ii) of the endothelial cells along the near side wall in static conditions (D) and in perfused channels at the fully developed (E) and stagnation point of the disturbed region (F). Scale for all frames: 25 μm.

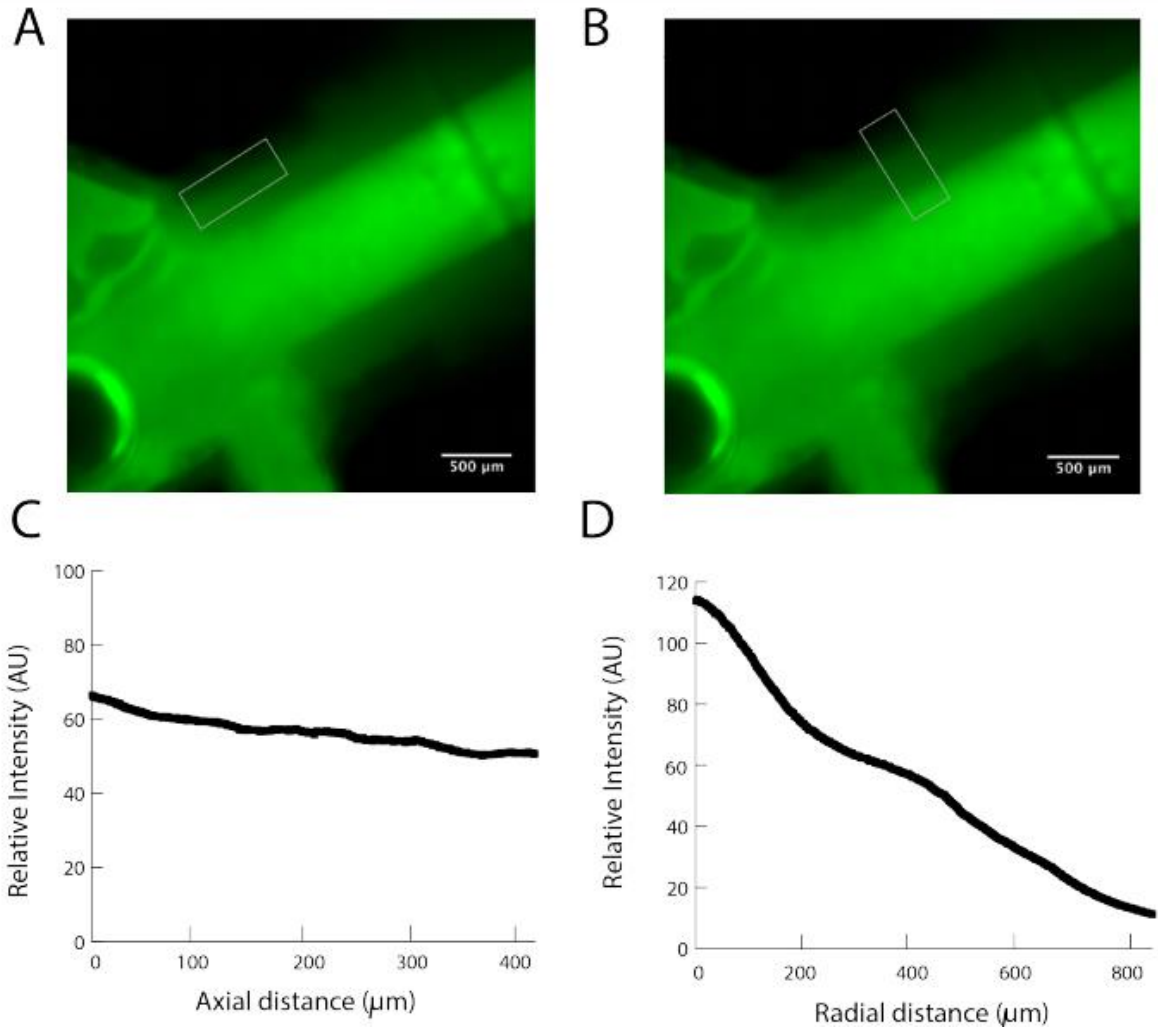**Verification Of Dextran Transport Across The Cell-Seeded Vessel.**

Figure F1. A) Dextran transport across the axial direction, B)Dextran transport across the radial direction, C) Relative intensity along the axial distance and, D) Relative intensity along the radial distance.

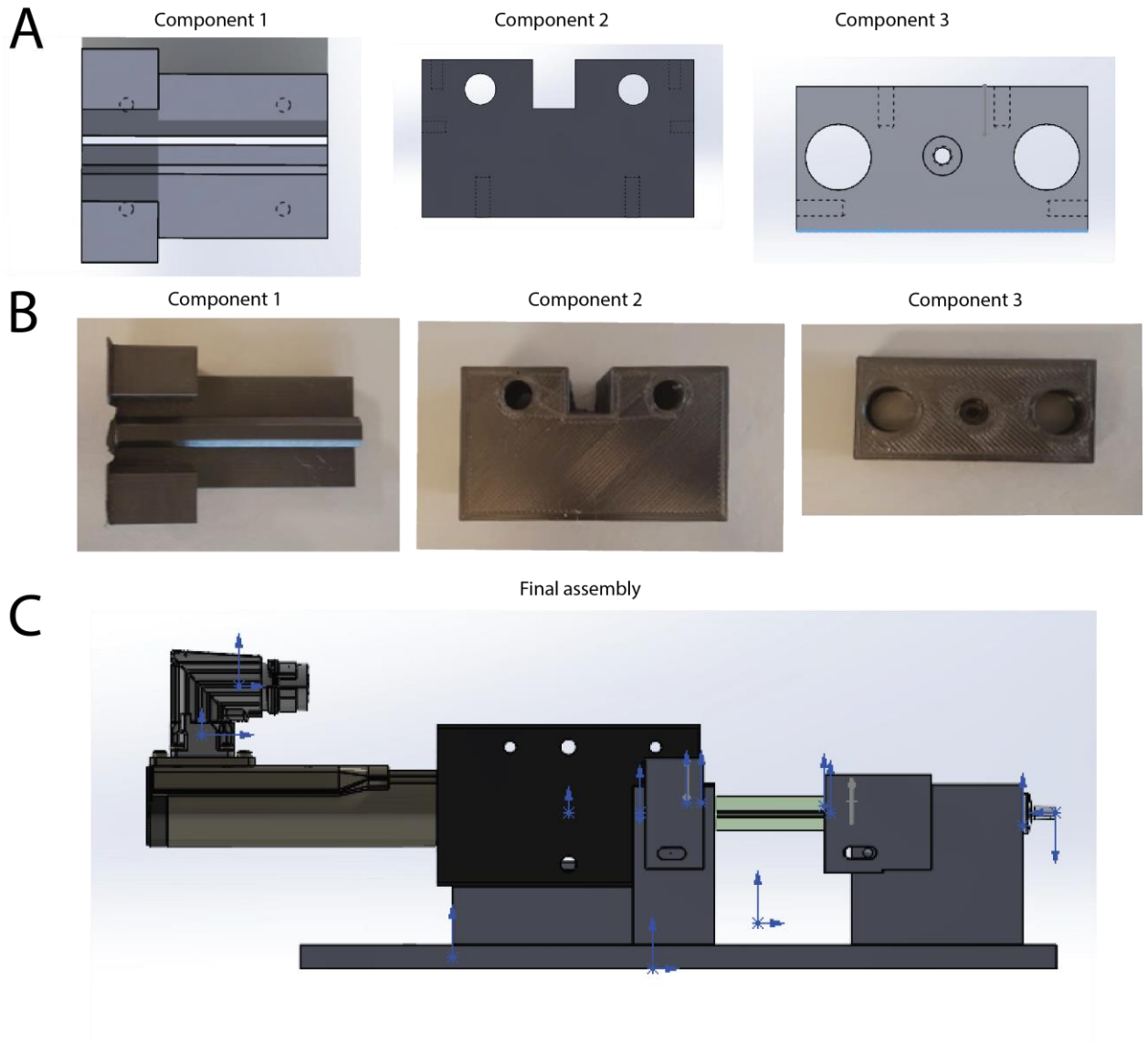**Final 3D Printed Components**

Figure G1. Device construction and assembly. A) CAD renderings (Solidworks) of the syringe components. B) Photographs of the printed components. C) CAD rendering of the linear actuator-syringe assembly.

Appendix H

Impact Of Disturbed Flow On Lumican Protein Expression

Figure H1. Rheometer setup used for the study of the impact of disturbed flow on protein expression